Perspective

Integrated Neurophotonics: Toward Dense Volumetric Interrogation of Brain Circuit Activity—at Depth and in Real Time

Laurent C. Moreaux,[1,*] Dimitri Yatsenko,[2,15] Wesley D. Sacher,[3,4,5] Jaebin Choi,[6] Changhyuk Lee,[6,7] Nicole J. Kubat,[1] R. James Cotton,[8,15] Edward S. Boyden,[9,10,11,12] Michael Z. Lin,[13] Lin Tian,[14] Andreas S. Tolias,[2,15,18] Joyce K.S. Poon,[5,16] Kenneth L. Shepard,[6] and Michael L. Roukes[1,3,4,17,*]

[1]Division of Physics, Mathematics and Astronomy, California Institute of Technology, Pasadena, CA 91125, USA
[2]Vathes LLC, Houston, TX 77030, USA
[3]Kavli Nanoscience Institute, California Institute of Technology, Pasadena, CA 91125, USA
[4]Division of Engineering and Applied Science, California Institute of Technology, Pasadena, CA 91125, USA
[5]Max Planck Institute for Microstructure Physics, Halle, Germany
[6]Departments of Electrical Engineering and Biomedical Engineering, Columbia University, New York, NY 10027, USA
[7]Center for BioMicrosystems, Brain Science Institute, Korea Institute of Science and Technology, Korea
[8]Shirley Ryan AbilityLab, Northwestern University, Chicago, IL 60611, USA
[9]Howard Hughes Medical Institute, Cambridge, MA, USA
[10]McGovern Institute, MIT, Cambridge, USA
[11]Koch Institute, MIT, Cambridge, USA
[12]Departments of Brain and Cognitive Sciences, Media Arts and Sciences, and Biological Engineering, MIT, Cambridge, USA
[13]Departments of Neurobiology and Bioengineering, Stanford University, Stanford, CA 94305, USA
[14]Department of Biochemistry and Molecular Medicine, School of Medicine, University of California, Davis, CA 95616, USA
[15]Center for Neuroscience and Artificial Intelligence and Department of Neuroscience, Baylor College of Medicine, Houston, TX 77030, USA
[16]Department of Electrical and Computer Engineering, University of Toronto, 10 King's College Rd., Toronto, ON M5S 3G4, Canada
[17]Division of Biology and Biological Engineering, California Institute of Technology, Pasadena, CA 91125, USA
[18]Department of Electrical and Computer Engineering, Rice University, Houston, TX 77005, USA
*Correspondence: moreauxl@caltech.edu (L.C.M.), roukes@caltech.edu (M.L.R.)
https://doi.org/10.1016/j.neuron.2020.09.043

SUMMARY

We propose a new paradigm for dense functional imaging of brain activity to surmount the limitations of present methodologies. We term this approach "integrated neurophotonics"; it combines recent advances in microchip-based integrated photonic and electronic circuitry with those from optogenetics. This approach has the potential to enable lens-less functional imaging *from within the brain itself* to achieve dense, large-scale stimulation and recording of brain activity with cellular resolution at arbitrary depths. We perform a computational study of several prototype 3D architectures for implantable probe-array modules that are designed to provide fast and dense single-cell resolution (e.g., within a 1-mm^3 volume of mouse cortex comprising ~100,000 neurons). We describe progress toward realizing integrated neurophotonic imaging modules, which can be produced *en masse* with current semiconductor foundry protocols for chip manufacturing. Implantation of multiple modules can cover extended brain regions.

Massively Parallel Interrogation of Brain Activity

> Within the central nervous system, the events in each unit are not so important. We are more concerned with the interactions of large numbers, and our problem is to find the way in which such interactions can take place.—Edward D. Adrian (1926)

These final lines from Lord Adrian's Nobel lecture (Adrian, 1926) illustrate the extraordinary prescience of this researcher who first discovered neuronal spiking. He anticipated that understanding brain computation is not likely to be achieved solely by studies of individual neurons but instead by observing coordinated interactions of neurons and their collective activity patterns.

Realizing instrumentation to monitor population activity within the brain with single-neuron resolution is a profoundly difficult challenge; Figure 1 provides a sense of the scale involved. The slow rate of technological development in neuroscience is elucidated in Figure 2; it charts the evolution of our ability to simultaneously resolve and track the activity of a multiplicity of neurons *in vivo*, over the six decades since the invention of whole-cell recording (Stevenson and Kording, 2011). Today's state-of-the-art technology permits simultaneous, full bandwidth recording *in vivo* in awake rodents from multi-shank neural probe modules, each with up to 1,024 channels (Rios et al., 2016; Shobe et al., 2015). With implantation of multiple probes of these types, many thousands of neurons are now being simultaneously recorded (Steinmetz et al., 2019). Although it is unequivocal that these advances
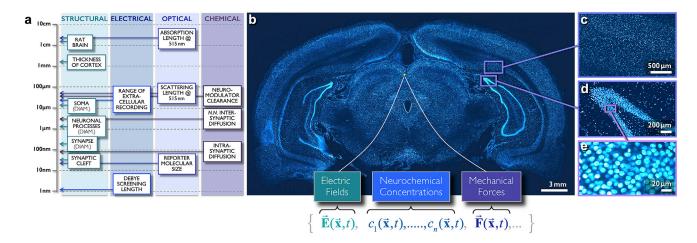
Figure 1. Brain Complexity, "Brain Fields," and Structural Length Scales Vis-à-Vis Cell-Body Location, Density, and Heterogeneity in the Rodent Brain
Strong light scattering and absorption in brain tissue make it extremely difficult to achieve dense, volumetric functional imaging with cellular resolution.
(A) Biophysical scales for electrical, neurochemical, and optical domain recordings and relative sizes of brain structures.
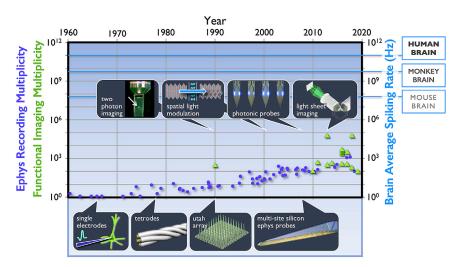(B) A ~2-μm-thick optical section of an adult rat brain slice, stained with a fluorescent nuclear stain, wet mounted, and imaged by large-scale serial two-photon microscopy. Beneath this image, we enumerate three "brain fields"—that is, domains of neural activity: the electrical, neurochemical, and mechanical.
(C–E) Cellular nuclear density at multiple scales (C, 500 μm; D, 200 μm; E, 20 μm), from the macroscopic down to the level of individual cells. Image credits for (B)–(E): L. Moreaux.

open exciting research frontiers, the number of observable neurons has continued to remain comparable to the total electrode count. This is consistent with the empirical observation that multi-site extracellular electrodes yield, on average, just one or two units per site, even with optimal spike-sorting algorithms (Marblestone et al., 2013). At this rate of development, another 90 years must elapse before the activity of an entire mouse brain, containing roughly 75 million neurons, will become observable (Figure 2). Clearly, we must significantly accelerate this rate of development.

This was a central aim of our proposal (Alivisatos et al., 2012) that eventually culminated in the launching of the US BRAIN Initiative (Bargmann and Newsome, 2014). Our initial vision, which still remains true, is that advances in nanotechnology, molecular reporters, and large-scale integration of semiconductor devices now make it feasible to precipitously upscale the rate of progress toward massively multiplexed interrogation of brain circuits (Alivisatos et al., 2012).

Here, we focus in more depth on these prospects. Our aim in this Perspective is not solely to identify ways to increase the total number of neurons that can be recorded from simultaneously. Instead, we explore the possibility of achieving *dense* recording from within a targeted tissue volume to ultimately achieve complete interrogation of local brain circuit activity. We use the word *interrogation* to denote recording and direct causal manipulation of a brain circuit's individual neurons by the application of patterned, deterministic stimulation with single-neuron resolution. To achieve this, we are pursuing a new approach, which we term *integrated neurophotonics,* that offers significant potential for accelerating progress toward Lord Adrian's vision. This technological path offers the prospect of dense functional imaging of neuronal activity in highly scattering neural tissue, providing cellular-scale resolution at arbitrary depths in the brain. Our approach is based on implanting an entire lens-less imaging system *within the brain itself* by distributing dense arrays of

microscale photonic emitter and detector pixels (hereafter, E-and D-pixels) positioned on a 3D spatial lattice (Roukes, 2011; Roukes et al., 2016). These pixel arrays are integrated onto narrow silicon shanks (needles), which leverage recent advances in silicon-nanoprobe-based fabrication (Rios et al., 2016; Shobe et al., 2015; Steinmetz et al., 2018). Used with functional molecular reporters (Andreoni et al., 2019; Chen et al., 2013; Lin and Schnitzer, 2016) and optogenetic actuators (Boyden, 2011; Miesenböck, 2011), this novel instrumentation offers the prospect of approaching the interrogation of *all neuronal activity* from within a 1-mm^3 volume (~100,000 neurons in mouse cortex). The approach leverages recent breakthroughs in molecular reporters that can enable multimodal and multi-physical sensing (Figure 1B), advances in optogenetic actuators that enable optical control of neural activity, and the genetically encoded delivery of molecular reporters and actuators that provide specificity of cell type. Further, the methodology is potentially scalable—multiple modules can be tiled to densely cover extended regions deep within the brain. We anticipate that this will ultimately permit interrogation —that is, simultaneous recording and patterned stimulation of millions of neurons, at arbitrary positions and depths in the brain—to unveil dynamics of neural networks with single-cell resolution and specificity of cell type. Like their contemporary counterparts for highly multiplexed electrophysiology (Ephys), ultranarrow photonic neural probes perturb brain tissue minimally given their small cross sections and passivated surfaces. They impose negligible tissue displacement upon implantation while dissipating low power during operation—comparable to today's active, multi-site Ephys probes that also employ complementary metal-oxide-semiconductor (CMOS) technology. And, importantly, they offer near-term prospects for wide deployment to the neuroscience research community, as they are mass producible by well-validated semiconductor foundry (microchip-production factory) methods.

Figure 2. Evolution of Recording Multiplicity for Electrophysiology and Functional Imaging Vis-à-Vis Overall Brain Activity (Spiking Rates)
(Left ordinate) Violet dots: the evolution of multiplicity for individual electrodes, implantable multi-site probes, and single multi-probe modules since the invention of whole-cell recording (Stevenson and Kording 2011; Steinmetz et al., 2018). Green triangles: also shown are recording multiplicities for single- and multi-photon functional imaging (from Lecoq et al., 2019) and light-sheet microscopy (Ahrens et al., 2013; Chen et al., 2018). For a current review of recording capabilities with multi-photon techniques, see Lecoq et al. (2019).
(Right ordinate) To compare the evolution of the technology against large-scale volumetric activity, we show the average spiking rate over entire brain—estimated as the product of the number of neurons and the brain average firing rate per neuron (∼2 Hz).

CONVENTIONAL ELECTROPHYSIOLOGY

Background: Intracellular versus Extracellular Ephys

Intracellular or *whole-cell* recording was pioneered by Hamill et al. in 1981 (Hamill et al., 1981), and this technique has remained the gold standard in Ephys. Its singular advantages are its high signal-to-noise ratio (SNR), the ability to directly target specific cells, and the important ability to deduce connection strengths between neurons directly, in what are often termed *multi-patch* (i.e., multi-electrode) experiments. However, there are significant technical challenges associated with whole-cell recording, particularly *in vivo* (Hulse et al., 2016). These arise from the delicate manipulations involved in patching that prevent upscaling the technique to enable simultaneous recording from more than roughly a dozen neurons, the practical limit achieved by today's expert practitioners (Jiang et al., 2013, 2015; Perin et al., 2011). Recent efforts have focused on the automation of patching protocols (Kodandaramaiah et al., 2012), but these have not yet yielded a substantial increase in the multiplicity of simultaneous whole-cell recording.

Extracellular electrophysiological recording, as first pioneered by Lord Adrian, is more amenable to upscaling. Microwire electrodes in twisted pairs ("stereotrodes") (McNaughton et al., 1983) and quadruples ("tetrodes") (Reece and O'Keefe, 1989) enable single-unit recordings from several adjacent neurons (Gray et al., 1995) when combined with spike-sorting protocols such as those first developed by Gerstein and Clark in 1964 (Gerstein and Clark, 1964). Over the past several decades, arrays of tetrodes have been successfully employed to observe patterns of activity over distributed regions of the brain (Wilson and McNaughton, 1993). However, scaling upward to the regime of thousands of channels has proven challenging.

ELECTRICAL RECORDING: THE PRESENT STATE OF THE ART

In 1970, well prior to the development of tetrodes, Wise et al. first pioneered use of silicon-based microfabrication techniques to upscale extracellular recording multiplicity (Wise et al., 1970).

Here, by *multiplicity* we mean the number of active neurons that can be simultaneously resolved and recorded. Massively multiplexed silicon neural probes have since been widely validated (Wise et al., 2008), commercialized, and upscaled to permit multiplexing of hundreds of recording sites within an individual probe (Berényi et al., 2014). However, despite the technology's potential and the advances made, the multiplicity of extracellular recording from an individual probe or multi-shank probe module has increased only by a factor of two roughly every 7 years over the past 60 years (Figure 2). As mentioned, silicon neural probes have recently been upscaled to contain more than 1,000 simultaneously active, full bandwidth recording electrodes within a single functional multi-probe module. Here, nano-fabrication methods permitting nanowire interconnects along the shanks enable the attainment of narrow shank cross sections (Rios et al., 2016; Shobe et al., 2015; Steinmetz et al., 2018) that are comparable to the diameter of tetrodes (typically, ∼35 μm) that permit chronic implantation. The expectation here is that (cross-sectional) size matters.

To evaluate the practical and ultimate limits of the recording multiplicity attainable with multi-site electrophysiological recording, the physical origin of extracellular currents and potentials must be considered. Extracellular currents arise from the activity of ion channels and pumps occurring both at soma and at neural processes. The slow spatiotemporal evolution of the local field potential (LFP) arises from ion exchange between soma, processes, synapses, and their extracellular environment—that is, throughout the vast regions over which neural processes extend. By contrast, rapid local waveforms arising from spiking are dominated by much faster somatic ion currents (Berényi et al., 2014; Buzsáki, 2004, Buzsáki et al., 2012). Spike-sorting protocols with multi-site electrodes take advantage of the latter; they permit separation and extraction of the fast temporal activity of individual *units* (arising from single-neuronal spiking) from the LFP signals (that arise from complex, ensemble-average, multi-neuronal activity). Recently, the effectiveness of spike-sorting protocols in various experimental contexts have been assessed qualitatively (Marblestone et al., 2013). This meta-analysis of their empirical limits is surprising.

Its conclusion is that while future improvements might, in principle, yield up to ten neurons per electrode for multi-site probes, experiments today typically yield a recording multiplicity that is smaller (i.e., much closer to 1:1). In other words, on average, one electrode is required for every neuron recorded. An important caveat here is that the activity of the brain region probed matters; regions with sparse activity will yield smaller multiplicities that can be obtained from regions with less-sparse activity.

This low multiplicity obtained from most multi-site Ephys recordings has important practical implications, both for the potential level of scale-up (multiplexing) that is attainable and for the likely density of neuronal coverage that is practicable. Scaling up the number of recording sites with 3D multi-shank architectures was first demonstrated in the 1990s (Campbell et al., 1991; Hoogerwerf and Wise, 1994). To minimize perturbation of brain activity, the consensus seems to be that implantable probes should altogether volumetrically displace only a fraction of a percent of neural tissue (Marblestone et al., 2013). However, this asserted limit is just an estimate; controlled, direct, and systematic studies have not yet been carried out.

Najafi and Wise first explored the possibilities for massively upscaling the recording multiplicity of silicon-based multi-site neural probes for Ephys (Najafi et al., 1990). They consider the mechanical robustness of silicon probes and conclude that to readily permit penetration of the pia, shanks 5–10 mm long (permitting access to deep brain structures in small mammals) should maintain a cross-sectional area of $\sim$200 μm^2 (e.g., 20 μm width $\times$ [at least] 10 μm thickness). Maintaining <1% volumetric exclusion of brain tissue for a 3D neural probe array constructed from such shanks would then impose a minimum inter-shank pitch of $\sim$140 μm, assuming a square grid architecture. With this configuration, and using the fact that state-of-the art, low-noise, single-unit recording requires an electrode geometric surface area of $\sim$180 μm^2 ($\sim$15 μm diameter for a circular electrode) (Ludwig et al., 2011), the maximum practical number of electrodes per unit volume of brain tissue can be estimated. Assuming each shank comprises a linear array of electrodes with a pitch of 1.5 times the electrode diameter (i.e., 22.5 μm center-to-center spacing), a maximum fill factor of approximately 2,100 electrodes/mm^3 is attainable. One cubic millimeter of mouse cortex contains approximately 100,000 neurons, and, being (overly) optimistic by assuming that a maximum of *two* units are extracted per recording site, we conclude that a volume coverage of only $\sim$4% of the neuronal population is the upper limit of attainable coverage. Again, this must be qualified that that coverage obtained will be dependent on the relative level of activity within the brain region probed.

These considerations can be revised somewhat in light of the new generation of ultra-flexible neural probes emerging from multiple laboratories (Jeong et al., 2015; Liu et al., 2015; Rousche et al., 2001). Thinner probes—which, for implantation, require removable stiffeners—could, in principle, permit closer probe spacing and, thereby, increase coverage of the neural population. Current efforts pursuing flexible probe technology focus on devices based on either polymeric materials or ultra-thinned silicon. The latter makes use of fabrication protocols permitting conventional semiconductors—usually considered brittle, inelastic materials—to be rendered extremely pliable by making

them extremely thin. Thinning the silicon substrate has two very significant benefits: it yields much thinner devices than their polymeric counterparts, and it enables use of state-of-the-art silicon CMOS circuitry (Navaraj et al., 2018; Shahrjerdi and Bedell, 2013). A recent analysis for these new flexible probe designs, in the same vein as that of Najafi and Wise, arrives at somewhat more optimistic conclusions (Kleinfeld et al., 2019).

Ultra-thinned CMOS silicon neural probes can thus be made almost an order of magnitude thinner than those estimated by Najafi et al. (Najafi et al., 1990), and this could reduce tissue displacement by a similar factor. Following the logic above, it could permit reducing shank spacing down to an $\sim$50 μm pitch. However, there are significant challenges to achieving reproducible implantation of such flexible 3D arrays. The requisite stiffeners, used to facilitate probe implantation, will likely displace a comparable amount of tissue as the somewhat thicker silicon probes that the flexible devices are intended to replace. Nonetheless, it is interesting to note that a 50 μm shank separation would be commensurate with the empirically deduced range of multi-site electrical recording (Buzsáki, 2004). The limitation on Ephys range arises from the combined biophysical effects of electrostatic screening in the ionic cerebrospinal fluid, the presence of other distributed sources of electrophysiological activity (which can raise the practical noise floor for detection), and the need to maintain sufficient SNR in extracellular recordings to permit efficacious spike sorting. Following the logic outlined above to ensure that volume exclusion of neural tissue is kept below 1%, a 10-fold increase in electrode density over the estimate above would permit volumetric coverage of up to 40% of adjacent neurons with an ultrathin probe array. But we emphasize that this is an *extremely* optimistic estimate; it is predicated on implanting an immense number of flexible probes (with their requisite stiffeners) without damaging adjacent tissue—a challenging task that seems unlikely to be achieved in practice.

Within the last few years, introduction of modern microelectronics technology, particularly through the development of the (rigid) Neuropixels probes and their counterparts, has resulted in significant upscaling of multiplexed electrophysiology (Jun et al., 2017; Steinmetz et al., 2019). Recent efforts by the Neuralink team (Musk and Neuralink, 2019) are also upscaling flexible probes that are packaged with application-specific integrated circuits (ASICs) for neural recording. The approaches used to connect the probes to the electronics today limit the number of achievable channels, but this will continually improve as packaging technologies evolve. This scaling, however, has largely been devoted to studying multiple or otherwise spatially disparate brain regions rather than to realize dense brain circuit coverage within a specific region. For this latter and very important challenge, practical and fundamental limits constrain the multiplicity of multi-site silicon probes for Ephys. These limitations result from the inherent locality of electrical recording, which, as mentioned, renders only one neuron (on average) accessible to any specific electrode within a multi-site array. For this reason, dense recording (full volumetric coverage of active neurons) seems unlikely to be achieved by conventional extracellular Ephys. Accordingly, it is natural to ask whether alternative technologies exist that might provide dense coverage of brain circuits with far fewer implanted elements. The key here

is to vastly increase the recording multiplicity obtainable from *each* recording element within an implanted multiplexed array, thereby minimizing volumetric displacement while massively up-scaling recording density and volumetric coverage. We will focus on this overarching challenge throughout of the remainder of this article.

BEYOND CONVENTIONAL EPHYS: FREE-SPACE FUNCTIONAL IMAGING

Functional imaging is an alternative approach to Ephys that enables both recording and localization of neurons in anatomical space. It also provides the very important added capability of specificity of cell type. However, as brain functions are not *optical* processes, neuronal activity must be *transduced* from its intrinsic domain (Figure 1B) into the optical domain; this is achieved by activity *reporters*. These reporters can be specific macromolecules or nanoparticles that comprise two moieties: one, the *sensor*, reacts to a targeted physical domain of local activity—be it electrical potential, molecular recognition, or mechanical forces; the other, the *chromophore*, provides optical functionality—it fluoresces at a particular wavelength when excited by an incoming photon within a specific band of wavelengths. In response to local neural activity from one of the aforementioned multi-physical measurement domains (Figure 1), the sensor, in turn, modulates the optical susceptibility of the chromophore. These bipartite reporters are then continuously interrogated optically to determine their instantaneous state of activity. Hence, local neuronal activity is directly reflected by changes in the chromophore's optical susceptibility.

FUNCTIONAL IMAGING AT DEPTH

Currently, functional imaging of neuronal activity in the rodent cortex is widely achieved using free-space, multi-photon, laser-scanning microscopy (Denk et al., 1990; Lecoq et al., 2019) of brain tissue that is labeled by molecular reporters (Grienberger and Konnerth, 2012). This combination readily provides cellular resolution of neural activity. Among such reporters are exogenous synthetic molecules, providing no cellular specificity, or genetically encoded proteins that, as described below, provide cellular specificity through restriction of their expression to specific cell types.

Free-space, two- and three-photon, laser-scanning microscopy (Denk et al., 1990; A.S.T., personal communication) together with fluorescent calcium reporters (Chen et al., 2013) enable functional imaging with subcellular resolution. However, at increasing depths within the brain, scattering and absorption ultimately preclude delivery of ballistic (i.e., unscattered) light with sufficient intensity and focus to achieve single- or multi-photon excitation of specific reporter-labeled neurons. The ultimate depth of delivery is limited by the optical attenuation length, $L_A \sim 1 / (L_{sc}^{-1} + L_{ab}^{-1})$, where L_{sc} and L_{ab} are the wavelength-dependent scattering and absorption lengths, respectively (Wang et al., 2018). Further compounding this is the challenge of extracting the information-bearing visible-wavelength fluorescent photons emitted by reporters. They are even more strongly scattered; L_A at green wavelengths is $\lesssim 100$ μm (Figure 6A). This results from

Mie scattering (Bohren and Huffman, 2004), which is predominant in this regime; it greatly diminishes the photon yield available to free-space optics placed *outside* the brain. Accordingly, even state-of-the-art three-photon functional imaging provides cellular resolution solely at depths less than ~1.7 mm (Ouzounov et al., 2017). Despite significant effort and investment, the growing consensus among experts is that this range is unlikely to be extended much further. All current methods for free-space imaging are therefore applicable solely at rather shallow (<2 mm) tissue depths (e.g., cortex) or to transparent organisms (e.g., zebrafish larvae).

Microendoscopy and Microfiber-Based Imaging

The complications outlined above have motivated the development of *microendoscopy*. This method employs an optical fiber implanted in targeted brain regions, sometimes with a miniature lens or prism, to achieve, for example, calcium functional imaging at the fiber's distal end via one-photon (1p) or two-photon (2p) fluorescence excitation (Liberti et al., 2017; Zong et al., 2017). Although such direct implantation resolves the issue of light delivery and recovery from deep within the brain, the approach has several limitations: (1) imaging is achieved only within the optical plane near the endoscope tip, (2) tissue along the path of implanted cannula/fiber (typically 0.3–2 mm diameter) is destroyed, and, hence, (3) current implementations of this approach do not permit functional imaging along extended vertical regions (e.g., multiple cortical layers) simultaneously. Accordingly, the approach is generally feasible only for measurements around the fiber/lens tip, using direct CMOS imaging (Inscopix, https://www.inscopix.com) or confocal laser microendoscopy (Mauna Kea, https://www.maunakeatech.com). Finally, (4) it seems unlikely that this method can be scaled up to achieve the dense volumetric coverage of neural activity that we consider here.

Another strategy, closely related to the integrated neurophotonics paradigm described herein, involves use of implantable tapered optical fibers patterned to enable multi-point illumination. These are coupled to an external laser source to enable passive, multi-point brain illumination at depth (Pisanello et al., 2014, 2017). By adjusting the incident light angle at the input fiber facet, various optical modes within the fiber can be addressed. A number of these modes are preferentially coupled to patterned optical windows along the length of the tapered fiber, so modal selection enables, in turn, site-selective light delivery. Similarly patterned tapered optical fibers can also permit passive local collection of light from a small number of sites along the fiber when coupled to an external photodetector (Pisano et al., 2019). Here again, microscale structuring of the fiber permits modal selectivity of the collected light. This approach enables depth profiling by fluorimetry for structures in close proximity to the fiber. This approach has recently been combined with a multi-electrode array (Sileo et al., 2018) and, more recently, a wireless system (Emara et al., 2019).

These advancements provide considerable advantages over conventional optical fibers, including the smaller, tapered form factor that is more amenable to tissue insertion, as well as finer-scale light delivery (i.e., finely patterned multi-point sources of light). A drawback, particularly for photodetection, is the fact that the brain interrogation area achievable by this approach is

restricted to cells in close proximity to the fiber. Also, the passive light collection used in this approach (i.e., guiding photons from the light source within the brain via an optical fiber to an external photomultiplier) differs from the active, highly multiplexed *in situ* light collection employed for photonic neural probes in our work, described below. However, the results of Pisanello et al. (Pisanello et al, 2014) represent an early and important validation of the new paradigm of implantable imaging systems with micro-scale dimensions. However, as tapered/window-bearing fiber fabrication is carried out one by one, this technology is not directly compatible with foundry-based mass production. It thus appears difficult to adapt this approach to permit the massive upscaling of multiplicity required to enable dense, volumetric-scale interrogation of brain activity over extended brain regions that we envisage here.

STATUS QUO: LARGE-SCALE, VOLUMETRIC FUNCTIONAL IMAGING

One prominent recent example of large-scale volumetric functional imaging *in vivo* is the multi-institution IARPA MICrONS project. In this effort, functional calcium imaging of all excitatory neurons expressing GCaMP6 within an $\sim$1 mm^3 volume spanning the mouse primary visual cortex and higher visual areas was obtained using a wide-field *mesoscope* (Sofroniew et al., 2016; Walker et al., 2019). For each mouse studied, multiple scans tiling the visual areas and cortical layers were obtained; these comprised many imaging planes acquired at a spatial resolution of 0.4 μm/pixel and a temporal resolution of 6.3 Hz. More than 5,000 neurons were imaged simultaneously, thereby enabling functional characterization of approximately 70,000 cells within each mouse. Once functionally imaged, the mice were sectioned and imaged by electron microscopy (EM) with nanometer-scale resolution at the Allen Institute for Brain Science. For one mouse, sectioning and imaging the complete $\sim$1 mm^3 volume spanning these regions by EM was performed. The EM data were subsequently provided to Princeton University, where the separate sectional images were aligned, segmented (to identify every soma, axon, dendrite, and synapse of the $\sim$100,000 cells within this tissue sample), and reconstructed in 3D. This combination of dense functional imaging and EM-based anatomical reconstructions within the same tissue volume is an important first step toward understanding relationships between the structure and function of neural circuits. Such efforts will ultimately permit the deciphering of circuit-level mechanisms that connect brain computations with behavior.

MOLECULAR REPORTERS AND OPTOGENETIC ACTUATORS

To date, the most widely employed approach for functional imaging involves intracellular calcium (Ca^{2+}) sensing (Charpak et al., 2001; Yuste and Katz, 1991). The temporal evolution of intracellular calcium concentration provides a robust proxy for direct electrophysiological measurements (Charpak et al., 2001; Ding et al., 2017; Moreaux and Laurent, 2007), but the approach has important limitations (Moreaux and Laurent, 2007). These molecular reporters operate by sensing the calcium
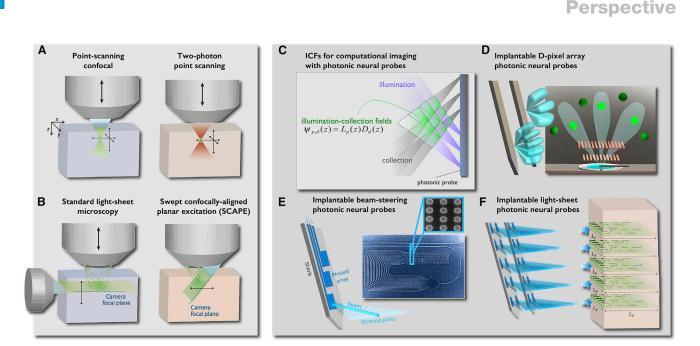
influx to the cell following an action potential; the resulting change in concentration modulates binding of the calcium to the reporter's calcium sensing moiety and, thereby, induces a change to the optical susceptibility of its chemically attached chromophore. The resulting stereotypical fluorescent transient that results is interrogated optically to provide a "report" on calcium influx after the neuron fires (Moreaux and Laurent, 2007, 2008). This has become widely adopted (Grienberger and Konnerth, 2012; Yuste, 2010) owing to the development of the excellent new class of fast optogenetically based calcium reporters exemplified by GCaMP6 (Chen et al., 2013).

Optical stimulation of neural activity requires optogenetic actuators (Miesenböck, 2011). The most successful and widely deployed of these are derived from the Opsin family (Shichida and Matsuyama, 2009). Opsins are light-sensitive ion channels and pumps that transport specific ions across membranes in response to optical stimuli (Zhang et al., 2007; Boyden, 2011). Embedded within the cell membrane, these actuators can induce or block action potentials when irradiated with light within a specific wavelength band.

Genes that encode for these molecular reporters and optogenetic actuators are introduced into neurons, either by gene delivery methods using viral vectors or through genetic engineering to create transgenic animal lines (Luo et al., 2018). This process enables neurons to express exogenous GCaMP and opsins. Selective expression of optogenetic actuators and molecular reporters restricted to specific cell types is achieved through the use of promoters that provide specificity of cell type. This offers enhanced selectivity and enables controlled or sparse expression of optical reporters within brain tissue.

Advanced Calcium Reporters

One- and two-photon imaging of neurons expressing genetically encoded fluorescent reporters of calcium concentration has become widely adopted in neuroscience. This is because calcium signals are robust, with intracellular calcium rising dramatically in concentration in many neuron types as a byproduct of firing action potentials and because bright, high-dynamic range, fast, genetically encoded reporters can be created by fusing fluorescent proteins to well-known calcium-binding protein motifs. The widely employed GCaMP family of calcium reporters (Chen et al., 2013; Dana et al., 2019; Tian et al., 2009), for example, is based upon GFP. Modern versions of these reporters, such as GCaMP6 and GCaMP7, can reliably both report well-separated action potentials and enable estimation of the frequencies of fast series of action potentials. However, expressing a calcium reporter throughout a neuron results in fluorescent light not only being generated from cell bodies, which many investigators want to focus on, but also from neuronal processes (i.e., from any axons and dendrites that are also illuminated). As many axons and dendrites pass within an optical diffraction limit of a cell body, this can lead to neuropil contamination during dense brain circuitry imaging. In this situation, optical signals from nearby axons and dendrites contribute artifactual spikes to a cell body of interest and thus lead to artifactual activity correlations between neurons. Much effort has been invested in focusing or *patterning* light to improve the collection of calcium signals from specific cells. However, complementary recent

Figure 3. Functional Imaging Methodologies: Free-Space versus Implantable, Lens-less Photonic Neural Probes
(A and B) Free-space Microscopy. (A) Point-scanning methods: epifluorescence and confocal; two-photon. (B) Light sheet microscopy in transparent tissues (denoted by bluish blocks) and oblique confocal scanning (SCAPE) in opaque tissues (brownish blocks). Both (A) and (B) are adapted from Hillman et al. (2019). (C–F) Paradigm and components of photonic neural probes. (C) Concept of fluorescence interrogation voxels in integrated neurophotonics: illumination collection fields (ICFs), which are the spatial overlap of illumination angular-fields produced by micro-sized emitter pixels (E-pixels) with detector angular-fields of micro-sized photodetectors. ICFs are analogous to the point-spread function, or optical-transfer function, in conventional optical imaging. (D) An angle-selective single-photon avalanche diode (AS-SPAD) detector pixel (D-pixel) arrays, where each D-pixel is equipped with off-axis Talbot gratings to yield an angle-restricted detection field. The diversity in spatial frequency, phase, and direction in the Talbot gratings of each pixel allows maximally randomized spatial sampling of the tissue volume, allowing computational reconstruction. (e) Implantable beam-steering photonic probe. Using coherent light in the blue spectrum and an optical phased array, an implantable photonic probe enables microscale collimated beams to be scanned within brain tissue by optical spectral addressing. Combining spectral (beam scan-angle, k) and spatial addressing (pixel number, i.e., phase-array element) enables scanning at different addressable depths. (f) Implantable light-sheet photonic probes imaging within opaque tissue. Photonic probes deliver blue light sheets enabling 2D interrogation of fluorescently labeled neurons within selective and individually addressable planes. As photonic probes can be implanted at arbitrary depths, they provide access to regions that are impossible to image with free-space methodologies.

efforts have pursued what one might call *molecular focusing*—that is, fusing calcium reporters to protein motifs that will localize them preferentially within the cell body. Two recent efforts on such somatic localization fuse GCaMP calcium reporters to different proteins, including a coiled-coil peptide set that restricts GCaMP to the cell body (Figure 4A, lower panel) (Shemesh et al., 2020) and a protein that tethers GCaMP to ribosomes, which also restricts GCaMP to the soma (Chen et al., 2020). In both cases, neuropil contamination is significantly suppressed due to reduced axonal and dendritic GCaMP, while somatic GCaMP brightness remains high and its kinetics remain fast. This improvement serves to suppress incorrectly attributed spikes and artifactual correlations between neurons. These benefits are observed in the mouse brain, as well as in other species, and they enhance functional imaging with both 1p and 2p instrumentation (including microendoscopy). Thus, by lessening the reliance on optics for selecting information to be obtained from specific cells, these molecular focusing strategies help to clean up signals in a way that is complementary to optical focusing methods. This can facilitate the use of simpler, more scalable optical systems than currently employed for imaging of neural dynamics *in vivo*. This molecular focusing approach has also been applied to fluorescent reporters of transmembrane potential (Figure 4), as discussed in the following section.
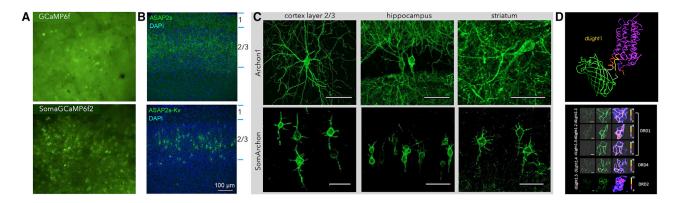
Voltage Reporters

As with optical calcium reporters, genetic approaches have also been used to design optical voltage reporters, often referred to as genetically encoded fluorescent voltage indicators (GEVIs). GEVIs are capable of reporting *subthreshold* voltage dynamics, which are not resolvable using extracellular electrodes placed adjacent to individual neurons (Herreras, 2016). Further, as with all of the genetically encoded optical reporters described here, genetic restriction—in terms of both cell type and subcellular location—can greatly facilitate data extraction and analysis (i.e., optical de-mixing and back-end computational analysis, as described below). To this end, in 2018, Daigle et al. reported the first somatically targeted GEVI, which was achieved by fusing ASAP2s to a cytosolic segment of a potassium voltage-gated channel (Kv2.1); this provided subcellular localization (Figure 4C) (Daigle et al., 2018). This approach was subsequently employed with ASAP3 and Archon to create ASAP3-Kv (Villette et al., 2019) and SomArchon (Piatkevich et al., 2019) (Figure 4B), respectively.

Additional parameters essential for optical de-mixing of GEVI signals include the reporter's *fluorescence amplitude* in response to single action potentials and its *molar brightness.* The largest relative fluorescence responses to individual action potentials are currently provided by the red-excitable

Figure 4. Restricted Subcellular Localization of Genetically Engineered Optical Reporters of Neural Activity
(A) Optical calcium reporters (GCaMP family). Representative time-averaged projection images of GCaMP6f (top) and its respective fusion protein variant (bottom) expressed in mouse dorsal striatum. Images were acquired with a 1p epi-fluorescent microscope. The fusion protein variant was identified in a screen designed to identify GCaMP fusion proteins with enhanced localization within 50 μm of the cell body with no effect on toxicity and GCaMP kinetics. Fusion of GCaMP6f to a *de novo* designed coiled-coil peptide to realize SomaGCaMP6f2 provides better SNR and fewer artifact spikes from neuropil than its non-fusion counterparts (bottom). Coiled-coil motifs, comprised of amino acid repeats that can assemble into complexes by "coiling" around one another via cognate sequence-structure pairing, were hypothesized by the authors to potentially slow diffusion of the GCaMP fusion proteins out of the cell body (Shemesh et al., 2020).
(B) Optical voltage indicator (ASAP reporters). Expression of ASAP2s (left) and ASAP2s fused to a cytosolic segment of the potassium voltage-gated channel Kv2.1 (right) in Cux2+ neurons in mouse cortex. ASAP voltage reporters are based on a circularly permuted GFP variant inserted within the voltage-sensitive domain of a voltage-sensing phosphatase (Daigle et al., 2018).
(C) Representative confocal images of neurons in cortex layer 2/3 (left), hippocampus (middle), and striatum (right) expressing Archon1 (top) and SomArchon (bottom). Scale bar, 50 μm (Piatkevich et al., 2019).
(D) Optogenetic dopamine reporters (dLight1 sensors). (Left) Simulated protein structure of the dopamine D1 receptor (DRD1)-based dLight1 sensor, color coded to denote key modules and components: inert DRD1 (purple), circularly permutated GFP (green), trans-membrane regions (red and yellow) and linkers (white and black). (Right) dLight1 plasma membrane localization in HEK cells (Patriarchi et al., 2018).

SomArchon ($\Delta F/F$ = 20%–50% per action potential) (Piatkevich et al., 2019) and the blue-excitable ASAP3-Kv ($\Delta F/F$ = 10%–30% per action potential) (Villette et al., 2019). Due to a difference in molar brightness between the two (0.076 mM^{-1} cm^{-1} for SomArchon versus 15 mM^{-1} cm^{-1} for ASAP3-Kv), illumination of ASAP3-Kv at ~25 mW/mm^2 at the focal plane achieves the same SNR as illumination of SomArchon at 400 mW/mm^2 (Villette et al., 2019). ASAP3-Kv and SomArchon thus provide two GEVI options at different wavelengths, with ASAP3-Kv requiring less power delivery to tissue.

One key drawback of GEVIs is the relatively fast sampling rate required. Actually, this drawback originates from the relative slowness of present-day instrumentation; fast-responding GEVIs, such as Ace-NeonGreen or ASAP3, require sampling rates of >500 Hz dynamics to optimally track their fast temporal response (Gong et al., 2015; Villette et al., 2019). Used in conjunction with 2p excitation, the instrumentation's sampling rates restrict the number of points that can be sampled over a spatially limited plane given the rather slow, serial nature of 2p microscopy (Villette et al., 2019; Wu et al., 2020). By contrast, genetically encoded calcium reporters respond to calcium transients triggered by action potentials that last for >100 ms. For these slower responding reporters, frame rates of 15 to 30 Hz are sufficient to track reporter dynamics.

Integrated neurophotonic probes offer the possibility to record GEVIs "at speed," given their intrinsically fast temporal dynamics, which (as described below) are sufficiently fast to follow even the nanosecond-scale temporal decay of the chromophores (Choi et al., 2019). In addition, because light from neurophotonic probes is much more strategically delivered within the illuminated tissue volume, background epifluorescence is reduced compared to free-space 1p methodologies (Segev et al., 2017; Sacher et al., 2020).

Neurochemical Reporters

The development of genetically encoded, intensiometric, and ratiometric fluorescence-based neurochemical reporters makes it possible to perform direct, long-term, and chemically specific functional imaging of neurotransmitters and neuromodulation dynamics. A variety of targets are now accessible, including dopamine, norepinephrine, serotonin, melatonin, and opioid peptides (Leopold et al., 2019; Oe et al., 2020; Patriarchi et al., 2018; Sun et al., 2018). Generally speaking, there are two main design approaches used to develop neurochemical reporters that involve G-protein-coupled receptor (GPCR)-based reporters and periplasmic binding protein (PBP)-based reporters, respectively (Andreoni et al., 2019; Leopold et al., 2019; Ravotto et al., 2020). A recent example of the former, the GPCR-based dLight1 chemical reporter family (Patriarchi et al., 2018), couples conformational changes of inert human dopamine receptors to changes in the fluorescence intensity of circularly permuted GFP (cpGFP) (Figure 4D, left). This provides a direct readout of dopamine kinetics with broadly tunable affinity and dynamic range, relatively rapid kinetics (10 ms on and 100 ms off), and fast temporal resolution. This reporter matches the performance of electrochemical methods for detecting monoamines while also providing subcellular resolution and molecular specificity. Additionally, the presence of the dopamine receptor transmembrane domain provides cell membrane targeting (Figure 4D, right).

In addition to GPCRs, bacterial PBPs have also been adapted for use as scaffolds for engineering small molecule reporters. Their use exploits the conformational change that occurs following binding of small molecules by its ligand binding domain (Leopold et al., 2019), sometimes referred to as a "Venus Fly-trap" domain (by analogy), which shares similarity with binding domains of many eukaryotic chemical receptors (including GPCRs) (Acher and Bertrand, 2005; Felder et al., 1999; O'Hara et al., 1993). As with GPCR-based reporters, when coupled to a chromophore, this conformational change can be translated into a change in the chromophore's optical susceptibility and, thus, its fluorescence (Leopold et al., 2019). PBP-based neuro-chemical probes, which include probes for glutamate (iGluSnFR), GABA (iGABASnFR), acetylcholine (iAchSnFR), and serotonin (iSeroSnFR), are brighter and have larger dynamic range, lower affinity, and faster kinetics compared to GPCR sensors. These attributes may mitigate problems such as buffering of native chemistry within the cytosol and interference with endogenous receptors (Marvin et al., 2018, 2019).

The optical cross sections of these chemical reporters are now similar to those of GCaMP reporters; hence, future advancements in subcellular targeting (for example, dendritic targeting of dopamine sensors) offer significant further potential for new insights. As the toolbox of genetically encoded optical reporters continues to grow, combining them with other reporters for simultaneous measurement of different functional readouts becomes a way to dissect multi-physical information processing within brain circuits occurring in diverse physical domains (Figure 1). With the development of red-shifted dLight1 variants and the new classes of calcium and voltage reporters, use of a multicolor approach offers the possibility of investigating, in real time, the simultaneous correlated activity of neurotransmitters, neuromodulators, and spiking.

Chromophore Excitation
Currently, serial scanning methods based on 2p microscopy are widely employed to excite the chromophores within optical reporters. This involves simultaneous absorption of two photons to induce nonlinear excitation of the reporter. Subsequently, decay of the excited chromophore back to its ground state results in the emission of a fluorescent photon in the visible spectrum. Near-infrared excitation wavelengths are typically used for biological microscopy given their longer attenuation lengths (Figure 6A). However, as the 2p optical cross section is very small, extremely high photon density is required to induce 2p absorption. Accordingly, to achieve requisite intensities, 2p excitation requires use of a single, tightly *spatially focused* beam of pulsed light that is also *temporally focused* into femtosecond-scale pulses. To achieve volumetric sampling under these conditions, a serial point-scanning methodology becomes necessary. The typical 2p interrogation voxel, generally of order $\sim$0.5 $\times$ 0.5 $\times$ 2 μm^3, is thus scanned in 3D, one point at a time, to spatially map the activity-dependent fluorescence of reporters within an ensemble of neurons, one by one. Today's 2p microscopes employing state-of-the-art acousto-optic deflectors (AODs) provide down to $\sim$1 μs point-access time and optical spike detection in multiple neighboring cells ($\sim$20) (Villette et al., 2019). This approach currently permits routine mapping

of $\sim$400 neurons in a 3D volume of 200 $\times$ 200 $\times$ 100 μm^3 with the requisite SNR to track spiking activity via the resulting modulation of somatic calcium signals (Cotton et al., 2013; Grewe et al., 2010; Katona et al., 2012).

The aforementioned approach has two important limitations that greatly complicate attempts to scale it up to enable functional imaging of large neuronal ensembles over extended brain regions: (1) serial optical interrogation and (2) SNR degradation with depth. We discuss each in turn below.

Multiplexing Limits of Free-Space Optical Interrogation
Serial point-scanning optical techniques can provide subcellular resolution, but they have the significant disadvantage that the total number of scanned voxels is limited by scanner speed. This is exacerbated by the photometric requirement to dwell at each voxel long enough to collect enough photons to attain requisite SNR. Simultaneous use of multiple excitation beams has enabled multiplexing by in-plane parallelization of 2p microscopy with regular wide-field detection. In this implementation, each beam is encoded with specific binary amplitude modulation to identify the location where fluorescence is generated (Ducros et al., 2013). *Depth multiplexing* using four pulsed laser beams has also been developed; this has been successfully applied to mapping cortical activity in four optical planes at four different depths (Beaulieu et al., 2020; Cheng et al., 2011). While these approaches enable significant multiplexing, in practice only a relatively small number of beams can be implemented. The maximum benefit obtained is ultimately determined by the number of beams multiplexed, the laser repetition rate, the reporter fluorescence decay time, and the total optical power that can be absorbed by brain tissue without undue perturbation to neuronal activity (or the tissue itself).

SNR Limits to the Depth of Imaging
Scattering and absorption limit the ability to deliver ballistic (i.e., unscattered) light with sufficient intensity to achieve 2p excitation deep within the brain. Ultimately, absorption limits the depth of delivery; in the near infrared (NIR), the maximum attenuation length is L_A $\sim$500 μm (Figure 6A). To overcome this significant limitation, several approaches have been explored. In one, the instantaneous laser power is increased to enable deeper 2p excitation while the pulse repetition rate is reduced to minimize the average power delivered to the tissue. This approach enables recording neuronal activity in populations of L5 neuronal soma up to $\sim$800 μm deep (Mittmann et al., 2011). However, collecting the visible-wavelength fluorescence photons from brain tissue becomes especially problematic at increasing depths. For these photons, scattering becomes the predominant limitation, as described below.

Extending this approach to achieve even deeper functional imaging becomes increasingly challenging; among issues are the generation of out-of-focus fluorescence (even with moderate spatial confinement along the beam) and the onset of nonlinear photodamage in neural tissue. A recent alternative approach involves using longer excitation wavelengths in the near infrared around 1.6 μm. This becomes possible if three-photon absorption processes are harnessed, and remarkable progress in this area has been achieved (Horton et al., 2013). Here, the principal

complication is the *significantly* smaller three-photon cross sections for existing reporters; this imposes limits on the utility of this methodology, as much higher illumination intensities are required.

An alternative approach employs adaptive optical corrections to rectify wavefront aberrations arising from spatially inhomogeneous optical scattering and absorption in brain tissue (Yaqoob et al., 2008; Girkin et al., 2009). This can effectively restore optical resolution in the 2p modality and can significantly improve deep-imaging capability. The approach is contingent upon measuring and employing the precise *aberration matrix* for a large volume of heterogeneous tissue. This is a challenging prospect; it requires complex multi-point measurements and subsequent computations. As brain topology is dynamical, the correction matrix remains effective only for the interval over which tissue is, in effect, stationary. Future work will elucidate the realm of applicability of this approach.

Precisely Structured Illumination

To separate fluorescent signal sources, laser-scanning microscopy localizes the illumination in space and time. We term this *precisely structured illumination*. Other fluorescence microscopy modalities structure their collection fields, sorting emitted photons by the place of their origin. For example, in wide-field microscopy, signals are localized by focusing the emitted light to form a spatial image. When neither the illumination fields nor the collection fields can be structured with sufficient spatial and temporal resolution, fluorescent signals become mixed. In this case, computational approaches can be employed to separate or infer the underlying signals. Several recording and imaging modalities (including some fluorescence imaging modalities) use computational approaches to infer the image or optical signals from insufficiently structured illumination and collection.

In diffuse optical tomography (DOT), multiple spatially separated light emitters illuminate the tissue (usually one at a time), and the resulting scattered light is subsequently collected by optical detectors at many different spatial locations. In this modality, spatial resolution is increased by increasing the number of sources and detectors. This technique has yielded resolution of ∼4 mm for imaging blood-oxygenation-level-dependent (BOLD) effects through the skull (Dehghani et al., 2008; Wheelock et al., 2019). Time-dependent diffusive optical tomography (TD-DOT) approaches, in which the emitters are pulsed and the time of flight (ToF) of the photons is determined at each of the detectors, improves the imaging capabilities by allowing better separation of scattering effects from those resulting from absorption or fluorescence (Azizi et al., 2009; Painchaud et al., 1999; Puszka et al., 2013).

Light-sheet fluorescence microscopy (LSFM), also known as selective-plane illumination microscopy, is one example of a compromise in which some degree of structured illumination is maintained while achieving higher frame rates than are possible in a point-based laser-scanning system (Chen et al., 2014; Hillman et al., 2019). In LSFM, a thin sheet of excitation light is generated, either by cylindrically focusing a beam or by digitally scanning a Gaussian or Bessel beam (Keller et al., 2008; Mertz, 2011; Power and Huisken, 2017). The sheet is scanned linearly across the sample as fluorescence images are sequentially

collected perpendicular to the illumination plane. Focused imaging enables separation of the collected light. By stacking the sheet images thereby obtained, the desired volumetric image is formed (Huisken et al., 2004; Keller and Ahrens, 2015). A complication of conventional LSFM is its requirement for two orthogonal objective lenses that must be specifically positioned spatially. The associated geometrical constraints have limited application of the technique to quasi-transparent organisms (e.g., larval zebrafish, *C. elegans*, *Drosophila* embryos) (Ahrens et al., 2013; Chen et al., 2018), chemically cleared mammalian brains (Keller and Ahrens, 2015), and brain slices (Haslehurst et al., 2018). Recently, swept confocally aligned planar excitation (SCAPE) microscopy, an LSFM method requiring only a single objective, has been developed to circumvent these constraints. With SCAPE, *in vivo* calcium neural imaging has been demonstrated in mice (Bouchard et al., 2015; Voleti et al., 2019).
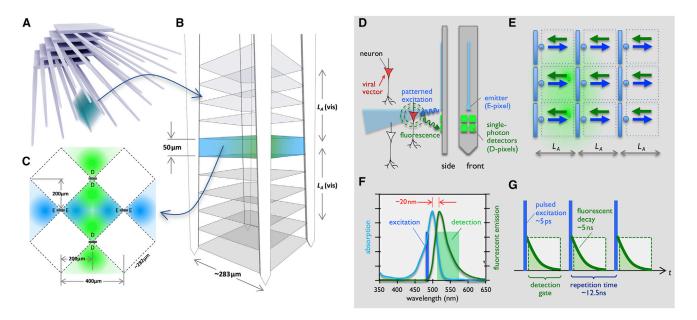
Acousto-optical Techniques

Another approach to improving imaging depth in scattering tissue is to employ ultrasound-modulated optical tomography (UOT), also known as acousto-optic imaging (Resink et al., 2012; Wang and Zhao, 1997). This has been used successfully to image absorption (Wang et al., 1995) and scattering (Kothapalli et al., 2007) at depth in tissue. Light is passed through tissue irradiated by an ultrasound beam. When it does so, it undergoes a frequency shift by multiples of the ultrasound frequency; by detecting the frequency-shifted light, resolution can be determined by the properties of the ultrasound (Wang, 2001). This tagging can be done at the source of emission. This approach is very similar to photoacoustic tomography (PAT) (Xu and Wang, 2006). In this case, acousto-optical effects are used to produce ultrasound upon optical illumination, and this ultrasound is used for imaging. While ultrasound is much more penetrative than light, these techniques are still limited in depth by absorption of ultrasound energy, which increases with carrier frequencies. Higher frequencies are required to improve wavelength-determined resolutions. While imaging is possible at depths up to several centimeters, cellular resolution is not attainable at depths beyond ∼3 mm (Liu and Li, 2020).

Implantable Microscopes

Several realizations of head-mounted microscopes for 1p and 2p calcium imaging in mice have proven the feasibility of fluorescence microscopy in compact form factors (Corder et al., 2019; de Groot et al., 2020; Ghosh et al., 2011; Jacob et al., 2018; Shuman et al., 2020; Skocek et al., 2018; Zong et al., 2017). To achieve imaging at depth requires implantation of the requisite GRIN lenses for these microscopes (typically 0.3–2 mm diameter), which results in a rather significant displacement of brain tissue. Extending these devices to support LSFM requires generating light sheets parallel to the surface of the brain at arbitrary depths while ensuring tissue damage is minimal after implantation of the requisite elements. In the study by Ye et al. (2016), a light sheet was generated by a microchip using a nanophotonic grating coupler, a rather thick (>100 μm) glass spacer element, and a metallic slit lens. In another demonstration, a sizable millimeter-scale prism coupled to a GRIN lens for light sheet delivery was implanted alongside a second

Figure 5. The Integrated Neurophotonics Paradigm via Photonic Neural Probe Arrays
(Left) Schematic representation of a 25-shank photonic probe array module.
(A) Architecture 1, described in the text and Figure 8A, is designed to record from 1 mm³ of mouse cortex.
(B) We decompose the brain region bounded by four adjacent shanks into "unit volumes" delineated by the repeat distance of E- and D-pixels along the shank.
(C) For Architecture 1, each unit volume is surrounded by a small ensemble of E- and D-pixels that illuminate soma and collect fluorescent photons in their proximity.
(Right) Time-domain interrogation of reporters.
(D) After an action potential, the optical susceptibility of calcium reporters within a labeled neuronal cell changes. This is read out by a short blue-wavelength excitation pulse that produces a green-wavelength fluorescence transient.
(E) Photonic probes operate in the mesoscopic regime where proximal emitters and detectors are separated by only a few scattering lengths. This circumvents issues with functional imaging in highly scattering brain tissue.
(F) The emission peak for a typical GCaMP family calcium reporter is separated by only ∼20 nm from its absorption peak, making continuous measurements essentially impossible; the excitation light is overwhelmingly more intense than the neuron's fluorescence. For this reason, we operate in the time domain to reject excitation light.
(G) Implementation of time gating to reject excitation light to enable detection of the much weaker neuronal fluorescence.

imaging GRIN lens (Engelbrecht et al., 2010). These examples remain limited by the significant tissue displacement of their implantable elements and their capability to generate only a single, static light sheet.
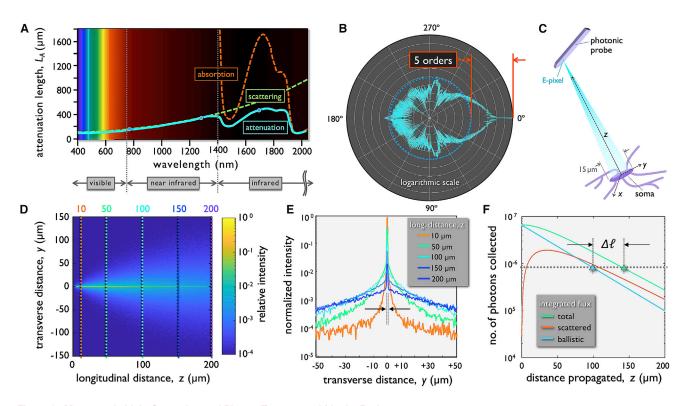
Emission-Related Limitations
As mentioned, scattering in neural tissue drastically suppresses the yield of fluorescence photons that can be collected outside the brain via free-space optics. Fluorescent photons originating deep from within the brain are multiply scattered as they pass through tissue to its periphery. To efficiently capture them, free-space collection optics with large angular acceptance (i.e., large field of view and low magnification) have been employed (Oheim et al., 2001). These can be rather costly and physically immense. To date, they have provided rather modest benefits.

THE INTEGRATED NEUROPHOTONICS PARADIGM

To surmount the limitations of free-space and endoscopic functional imaging described above, we have conceived of a new paradigm that we term *integrated neurophotonics.* It can provide the basis to enable fast and dense volumetric mapping of brain

activity. It leverages recent advances in integrated silicon nanophotonics, nanoelectronics, and optogenetics to enable massively multiplexed functional imaging arbitrarily deep within the brain. Employed together with optogenetic actuators and molecular reporters, photonic neural probe arrays—realized by integrating all elements of a lens-less imaging system onto ultranarrow implantable silicon shanks—can enable dense interrogation of brain activity with minimal tissue displacement (Figures 5 and 7). As such, it contains elements of many of the approaches described above, leveraging implantable CMOS electronics (as in scaled Ephys approaches), structured illumination (as in LFSM or scanning microscopy), and computational approaches to exact as much information as possible from scattered photon (as in diffuse optical tomography). However, in this paradigm the emitters and detectors are brought close to the fluorescent sources, producing finer structure in local illumination and collection fields to resolve local signals even in a highly-scattering medium such as brain tissue.

Photonic-probe-based interrogation is unique in its ability to circumvent the scattering limitations of brain tissue. This is achieved by distributing the imaging components—specifically, geometrically ordered arrays (*architectures*) of microscale photon emitters (E-pixels) and detectors (D-pixels)—within the

Figure 6. Mesoscopic Light Scattering and Photon Transport within the Brain

(A) Absorption, scattering, and attenuation in brain tissue versus wavelength (adapted from Horton et al., 2013).

(B) Forward Mie scattering in brain tissue is overwhelmingly forward directed. Polar diagram of the scattering of blue light (λ = 480 nm, unpolarized) from a sphere with radius r ~15 μm, and index difference Δn ~0.11 from its environment. This closely approximates scattering from a soma in extracellular media. Each concentric circle represents a 10-fold increase in intensity. As shown, the forward peak at 0° (cyan trace) is generally more than five orders higher in intensity than scattered light (adapted from Laven, 2020).

(C) Schematic depicting illumination impinging upon a neuron after propagating a distance, z, in scattering tissue. For simplicity, the E-pixel is idealized as a point emitter ($d = 0$)

(D) Heatmap showing beam intensity versus distance from the aforementioned microscopic emitter.

(E) Lateral beam profile for five distances from the emitter that are shown as dashed lines in (C). It is evident that the microscale beam remains highly collimated even 200 μm away from the emitter.
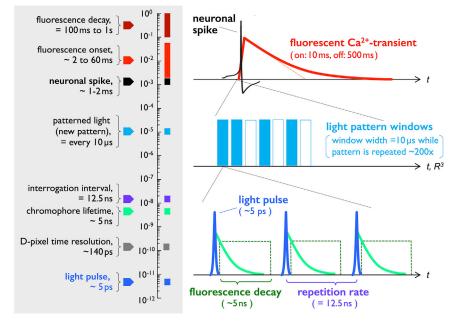
(F) Comparison between ballistic photons (blue trace) collected by the "neuron" (15-μm-diameter disc, representing a somatic cross section) as depicted (C), with those arriving after scattering (orange trace). The horizontal dashed line exemplifies that, because of strong forward scattering in the mesoscopic regime, a given total photon flux (green trace) for, e.g., a million photons can be collected a significant distance, $\Delta\ell$, further from the source than is the case considering only the ballistic contribution.

brain, separated only by distances of order a few times the optical attenuation length, L_A (Figure 5E). The depth limitation for photonic probe functional imaging solely arises from the readily engineerable probe length and the depth of their implantation. This new paradigm involves the integration of a lens-less imaging system onto narrow implantable shanks. It also requires the creation of new back-end hardware to control the instrumentation and stream the vast amounts of data it will produce. And it requires new and efficient computational algorithms that transform the immense cache of raw data the system produces into a succession of time-sequenced, cell-specific functional recordings of neuronal activity. Together, these elements form a complete and ultrafast lens-less functional imaging system with an implantable "front end" having microscale dimensions. A multishank probe module comprises an ordered array of shanks that can be readily implanted at arbitrary depths anywhere within the brain. These can be implanted as individual modules or as a coherently controlled module array that enables dense and extended volumetric coverage.

A FUNDAMENTAL CONCEPT: SOURCE LOCALIZATION IN HIGHLY SCATTERING BRAIN TISSUE

A pervasive mindset is that achieving cellular-level resolution of sources in diffuse media, even at modest distances, is impossible because (as the thought goes) light scattering in neural tissue quickly and completely randomizes the direction of propagating photons. These challenges, for example, lead to the limitations of conventional approaches—including 1p and 2p imaging, UOS, PAT, and DOT. For integrated neurophotonic systems, this problem is surmounted by positioning microscale emitters and detectors within the brain tissue separated by distances of order a few times L_A. This is schematically depicted in Figure 5E. This *mesoscopic regime* for light scattering governs the performance of photonic neural probe array architectures. Several concepts clarify the underlying physics and provide intuitive understanding of this regime. First, structural imaging with high spatial resolution is *not* required to achieve functional imaging. Instead, it is sufficient to simply obtain sufficient information for source

Figure 7. Temporal Scales and the Time-Domain Acquisition Protocol

The system's fastest timescale is the duration of individual E-pixel emission pulses (~5 ps) and the temporal resolution of the SPAD D-pixels (~140 ps). As mentioned, together they enable resolving the fast temporal decay of reporter chromophore fluorescence following an excitation pulse (~5 ns). Data acquisition sequences—a geometric pattern of pulsed, multiple-E-pixel light emission (5 ps), followed by a D-pixel acquisition window (~10 ns gate)–are repeated every 12.5 ns (80 MHz repetition rate). Given the 5 ns typical fluorescence lifetime of the reporter chromophore (green trace), this interval allows for a sufficient recovery period before the next interrogation. A specific light pattern is repeated as a train of ~800 data acquisition sequences are acquired and averaged; the stationary light pattern used during one ~10 μs data acquisition window is then changed for the subsequent 10 μs window. Thus, on the (relatively) slow timescale of a single action potential (~1–2 ms), several hundred light patterns can be imposed, each of which is repeatedly signal-averaged roughly 1,000 times to suppress photon statistics to enable acquisition of high SNR data and minimize energy deposited within the tissue.

separation and localization—that is, to be able to deduce the cellular origin of photons collected by the D-pixels for a diverse ensemble of illumination patterns. Our goal, in contrast to that of conventional imaging, is to track the functional activity of individual soma. To facilitate this process, it is critical to employ the latest generation of optogenetic reporters that are somatically localized (Piatkevich et al., 2019; Shemesh et al., 2020; Villette et al., 2019). They serve to preclude dilution or complete obfuscation of somatic fluorescence signals by contaminating background light that would otherwise be generated by the neuropil. We seek to faithfully track the fluorescent photons emitted from these somatically localized reporters; they convey information about each labeled cell's instantaneous state and activity. In this paradigm, we thus solely need to uniquely separate one neuron's information from that of adjacent soma. This criterion significantly relaxes the requisite spatial resolution, making resolution at the cellular scale (~15 μm) sufficient. Second, whereas imaging at high resolution unequivocally requires minimal scattering of a scene's photons to avoid distortion or degradation, source separation and localization requires only a moderately faithful extrapolation back to the particular soma from which the photons originate.

Figure 6 shows that while ballistic photons are indeed scattered over short propagation distances, this scattering is overwhelmingly dominated by small-angle scattering. Hence, even after multiple scattering events, fluorescence photons propagating within the mesoscopic regime largely remain forward directed, and it is thus feasible to trace their origin back to a distinct soma.

COMPUTATIONAL LENS-LESS FUNCTIONAL SOURCE SEPARATION AND LOCALIZATION

The raw data acquired from lens-less photonic-probe-array imagers require back-end computation to arrive at the desired infor-

mation. For this paradigm, the overarching question is whether it is possible to computationally de-mix the ensembles of simultaneously recorded somatic fluorescence signals. The answer is obviously affirmative if the individual soma are each separately and sequentially illuminated—this is precisely how random-access, point-scanning, multi-photon functional imaging is achieved. Similar issues have recently been encountered, and solved, for Bessel-beam-based functional imaging (Lu et al., 2020; Wu et al., 2020), where multiple soma can be simultaneously illuminated along the beam's path and contribute to the fluorescence signal. Here, the key is for our experimental instrumentation to provide sufficient spatial selectivity. By this we mean that the individual pixels' illumination and collection fields (Figure 3C) are geometrically reduced in scale to provide tight, microscopic spatial resolution. By sufficiently increasing what we term the *spatial diversity* of the pixels, we can circumvent the need for de-mixing, in the same manner as for other microscopy imaging modalities with microscopic, diffraction-limited point spread functions. However, increasing our system's spatial selectivity to enable this (ultimate) level of resolution requires an immense number of E- and D-pixels with very high spatial diversity that strongly restricts their individual angular ranges of emission and collection. Instead, we seek a more practical solution that maximally simplifies system architecture and complexity (and, ultimately, *cost*) while attaining the more relaxed imaging goal of simply achieving signal separation. We have carried out detailed computations of linear de-mixing for a variety of E- and D-pixel architectures that are summarized in Figure 8 and discussed below. These initial efforts show that relatively simple configurations can indeed achieve this goal (Yatsenko et al., 2020).

It is important to draw the distinction between inverse imaging (e.g., as achieved with DOT) and *source separation* and *source localization*, which are critical to functional imaging. The goal of inverse imaging is to obtain an image as a function of spatial
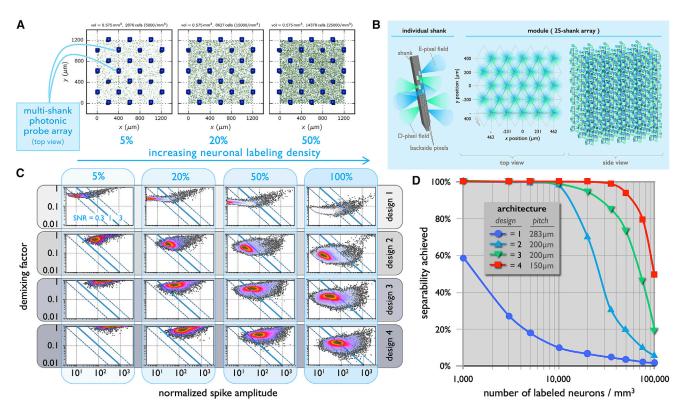
Figure 8. Computational Approach to De-mix Detector Photon Counts to Obtain Multiplexed Time Records of Individual Neuron Activity
(A) Schematic depicting a top view of one 24-shank photonic probe array module (design 1), implanted in a 0.558 mm^3 volume of mouse cortex that is labeled with increasing density.
(B) Schematic of a probe-array architecture (designs 2, 3, and 4) providing dense coverage.
(C) Family of results at various labeling densities for three photonic probe architectures.
(D) Summary of the evolution of separability with increasing labeling density for the three module architectures. Here, we assume SNR > 1 as the criterion for separability.

coordinates. If the image is of a population of cells each labeled with a fluorescent calcium indicator, it can be segmented to measure the calcium signals for its distinct spatial location; in this case, the signals are already separated based on their spatial origin. By contrast, signal separation refers to techniques that extract individual fluorescent signals from mixtures without ever producing an image. If many independent recordings are sufficiently made, each with differently mixed signals, special algorithms known as *blind source separation* (BSS) methods can isolate the individual voices from the overall cacophony (Comon and Jutten, 2010). This problem is related to the famous "cock-tail party problem" that our brain solves, quite successfully, when we listen to a friend tell a story in a noisy bar. In general, BSS is a difficult problem to solve; it relies on the innate proper-ties of the signals composing the mixture: their sparsity and syn-chrony, temporal structure, and amplitude distributions. Finally, *source localization* solves the problem of assigning a spatial location to a signal extracted by source separation. In our eval-uations through simulation, we focused on the necessary condi-tions for effective source separability.

The Formalism
We have developed a mathematical formalism and numerical code to explore a variety of possible system architectures and

quantitatively evaluate their performance for lens-less functional imaging. The ultimate metric for performance is signal separa-bility, and we must understand how this evolves as fluorescent labeling density is increased. We define it as the percentage of labeled neurons that can be de-mixed—that is, isolated and spatially localized, to provide separate activity time records from large ensembles of neurons interacting in realistic measure-ment scenarios.

For our initial effort, we set an ambitious target goal of recording, in real time, the activity of *all* neurons within a 1 mm^3 volume of mouse cortex, comprising ~100,000 neurons. Although even partial coverage will be transformational, we have identified several specific probe-array architectures that permit dense functional imaging (Figure 8B). Briefly, our computational approach involves, first, direct numerical simulation of photon propagation and scattering from spiking, fluorescently labeled neurons within a model of cortical tissue that captures the essen-tial physics. With a prescribed 3D system architecture input (which can be varied), the simulations then permit evaluation of the photon counts received at each D-pixel within the array. These arrive from the labeled and active neurons within the target volume, which fluoresce in response to a programmed va-riety of illumination patterns generated by the E-pixel arrays. With this simulated data in hand, the second step is to assess

the numeric properties of optical mixing to establish the feasibility of linearly de-mixing the acquired data to extract the functional activity of each individual neuron in the ensemble. The de-mixed output constitutes the desired collection of activity time records from each neuron within the targeted volume of brain tissue.

In Ephys, the spiking activity of individual neurons, termed *single units*, can be effectively isolated despite being mixed within a cacophony of many other signals picked up in multichannel electrical recordings. This de-mixing of spikes, or spike sorting, is possible given each neuron's precise and stereotypical spatio-temporal depolarization-repolarization pattern in the course of its action potential. These events are fast, on the order of 1–2 ms, and are separated in time by a refractory period; this further aids the ability of algorithms to recognize and isolate spikes.

By contrast, neuronal spiking activity measured optically with fluorescent calcium reporters is temporally blurred due to the relatively slow kinetics of both the intracellular calcium response and the calcium reporter binding. This blurring can both erase the separation between spikes in time and confound any distinguishing characteristics of individual neuronal responses. Further complicating this situation is the shot-noise limited nature of low-light imaging, which results in much lower SNRs than for Ephys recording. These challenges preclude direct application of standard Ephys spike-sorting algorithms for calcium imaging. Similar challenges exist for imaging with voltage reporters. Instead of spike sorting, for calcium-reporter-based functional imaging we employ modalities aimed at isolating individual cells optically by focusing the illumination fields (e.g., laser-scanning microscopy), focusing the collection fields (wide-field microscopy), or focusing both (e.g., confocal and light sheet microscopy). Even for relatively good optical isolation, additional linear de-mixing may be required to isolate cellular signals that are conflated with those of the neuropil. To achieve this, a de-mixing matrix inferred directly from the data, by methods such as BSS, is employed (Mukamel et al., 2009; Pnevmatikakis et al., 2016; Zhou et al., 2018). The aforementioned new classes of somatically restricted reporters help to greatly simplify these issues. For integrated neurophotonics, we employ *all* of the advances described above to enable lens-less functional imaging.

The Role and Importance of System Architecture

Architectures and subcomponents for photonic neural probes can be configured to provide varying degrees of spatial selectivity. The simplest instantiations, however, can be too coarse to directly isolate cell bodies optically. Yet the probe's illumination and collection fields (Figure 5E) can produce strong spatial gradients, thereby yielding distinct combinations of illumination intensities and collection probabilities from the arrays of E-pixels and D-pixels, respectively. Together, they generate high-dimensional and highly mixed optical responses. The total number of linearly independent signals (the rank of the mixing matrix) from a photonic neural probe is equal to the product of the number of D-pixels and the number of linearly independent illumination patterns employed. With hundreds of emitter and detector pixels implanted within a cubic millimeter volume of neural tissue, the number of such linearly independent measurements can be immense, reaching hundreds of thousands

and thereby exceeding the total number of cell bodies in the same volume.

The question then becomes: can the photon counts acquired by a D-pixel array, using optimal cycles of patterned illumination, be de-mixed computationally to isolate *every* neuron's optical signal? To resolve this, we simulate signal acquisition from a population of neurons within the (approximately) 1 mm^3 tissue volume embedding a photonic-probe-array module. Further, we investigate how signal separability is affected by both module architecture and the attributes of their constituent D- and E-pixels. To be specific, we systematically alter the number, shapes, and spatial diversity of the pixels. The latter determines the geometric arrangements of the illumination and collection fields of the individual detectors and emitters and determines the spatial selectivity that they provide as an ensemble (Figure 3C). For these different architectures and elements, the total fraction of neurons that can be effectively separated varies. To enhance separability, we also design specific algorithms to optimize the *illumination cycles* (i.e., sequences of emitter "on" times and the spatial patterns of light employed during a single acquisition window). Full details of this work are presented elsewhere (Yatsenko et al., 2020); here, we provide an overview of the computational procedure, prototype architectures explored, and the salient points we have gleaned. Model parameters are summarized in Table 1.

Architecture 1: Partial Separability

The first design we consider comprises 24 shanks, forming a square array with a pitch of 283 μm × 283 μm. (Figure 8A). Each of these shanks supports 72 E-pixels, arranged as nine separate rings, each comprising eight E-pixels. Along the length of the shank (z axis) and between these rings of E-pixels are opposite-facing pairs of D-pixels. In total, the design features 1,296 E-pixels and 288 D-pixels. The E-pixels measure 10 μm × 10 μm in size, whereas the D-pixels measure 10 μm × 50 μm. The rings of E-pixels and the pairs of D-pixels are arranged uniformly along the 400 μm length of the shanks. The E-pixels have Lambertian emission profiles, thereby illuminating with a cosine intensity distribution in all directions over the hemisphere normal to the shank surface. The individual E-pixel emission level was set to 20 μm, resulting in total average power of 0.125 mW. In Architecture 1, the D-pixels are receptive to all incident angles, resulting in a Lambertian collection profile. The total convex hull volume spanned by the shanks is 0.558 mm^3.

We then estimate the ability of the probe-array architecture to separate the acquired optical signals by first carrying out a Monte Carlo simulation of E-pixel array light emission, propagation, fluorescence, and D-pixel array detection. We start with the idealized case in which all fluorescence signals emanate from a number of discrete sources with a specified volumetric density. For example, these may be thought of as sparsely labeled cell bodies with the fluorescent reporters constrained within the soma. Although we model the cells as small spheres, all considerations below apply equally well to *sources* (neurons) with considerable geometric complexity as long as the optical signal they produce exhibits temporal coherence (i.e., appears as a single source distinct from other sources rather than a mixture of several sources with distinct spatial distributions).

Table 1. Computational Analysis

Parameter	Value
Photon scattering length, L_{sc}	50 μm
Photon absorption length, L_{ab}	1.4 cm
Anisotropy coefficient, g	0.88
Photons/joule (480 nm)	2.4×10^{18}
Effective optical cross section of a labeled neuronal soma	5×10^{-9} cm^2
Reporter resting/ maximum fluorescence levels	0.05
$\Delta f/f$ for a single action potential	40%
Calcium transient time constant	1.5 s
D-pixel detector quantum efficiency	0.65
D-pixel dark noise	300 counts/s
E-pixel emission level	20 μW/emitter

We model photon propagation by trajectory calculations that are limited by an absorption length, L_{ab}, a scattering length, L_{sc}, and a Henyey-Greenstein anisotropy factor, g, which accounts for the strong forward Mie scattering that occurs in brain tissue. These parameters are shown here.

Characteristics of the probe modules that are employed in these calculations—specifically, the E- and D-pixel densities and their angular profiles, as well as the probe array architectures—are fully described in the text. We assume the same transport parameters for both excitation and fluorescent light. Physical parameters used in these calculations vary minimally from the peak of the absorption band (480 nm) at the peak of the emission band (515 nm).

Parameters we employ for our signal separability calculations are also shown in the table; the ΔF/F value employed corresponds to the performance of new soma-restricted calcium indicators. The effective absorption cross section of a neuron at maximum fluorescence is estimated by assuming a uniform 50 μM somatic dye concentration within a spherical volume of 7 μm radius. This corresponds to 3.3×10^7 molecules per cell, a 2.3×10^{-16} cm^2 cross section for each fluorophore molecule, and a quantum yield of $\varphi = 0.6$. The E-pixel emission level is comparable to power commonly employed in other imaging modalities. We have validated it below threshold for tissue damage and phototoxicity by experiments both *in vitro* (brain slices) and *in vivo* (mouse) (Segev et al., 2017; Sacher et al., 2020).

Full details underlying these signal separability calculations are reported in Yatsenko et al. (2020).

The De-mixing Process

The relationship between the instantaneous fluorescence states of the ensemble of labeled neurons and the photon counts received by the D-pixel array is represented by what we term the *mixing matrix*. To permit interpretation of the data acquired from an experiment using a photonic probe module, we seek its inverse, the *de-mixing matrix*. It estimates the configuration and time records of fluorescent signals from the sources, given the photon counts acquired by the D-pixel array. In a real-life recording, the mixing matrix is generally unavailable. Accordingly, well-established numerical methods for BSS are used to estimate the de-mixing matrix directly from the data (Comon and Jutten, 2010). In our simulations, however, since we *impose* both the architecture and the source properties directly, we have complete knowledge of ground truth. In this situation, we can obtain the de-mixing matrix using a regularized pseudo-inverse of the mixing matrix. This allows us to evaluate the numerical properties of the mixing process, use it to subsequently iterate and optimize the effectiveness of various probe-array architectures and the characteristics (spatial diversity) of the E- and D-pixels they comprise, devise specific illumination patterns, and evaluate the results generated.

To carry out such optimizations, we examine the SNRs of simulated calcium spikes extracted from the signals de-mixed by a regularized pseudoinverse. Regularization allows estimating the de-mixed signals, the photon shot (quantal) noise in the de-mixed signals even when the mixing matrix is ill conditioned for inversion. The computation also yields channel cross-contamination levels that arise from the regularization procedure so that sources with excessive contamination can be excluded. When this contamination exceeds 1% of the de-mixed signal power for any of the fluorescent sources, we deem such sources inseparable from the signals of the surrounding population. We find that the fraction of such sources is negligible for most of the architectures we have explored. For the remaining unbiased signals, we compute the SNR of a single calcium spike, or the *de-mixed spike SNR*. Showing that an effective de-mixing matrix exists is a necessary but *insufficient* condition for demonstrating that numerical de-mixing is possible in the absence of a ground-truth mixing matrix. Here, we employ de-mixing effectiveness as a principal design criterion for evaluating possible photonic probe-array architectures.

Time-Domain Data Acquisition

Compared to the timescale of neuronal dynamics, our lens-less imaging system is *extremely* fast. Figure 7 shows the temporal hierarchy that applies to our paradigm.

We describe a typical temporal data acquisition sequence. For Architecture 1, we employ a cycle of 277 illumination patterns, in which specific collections of the 1,296 E-pixels switch on for just ~5 ps (i.e., just a fraction of the 10 μs light pattern windows) (Figure 7). After each light pattern pulse, D-pixel counts received are integrated for ~10 ns. The same pattern is repeated for ~1,000 times during the 10 μs light pattern window to permit significant averaging of the photon counts received during each 10 ns data acquisition window. This serves to suppress shot noise and thereby yield good SNR. The volumetric and temporal average light intensity irradiating the tissue is set to correspond to a level commonly employed for multi-photon imaging. The light patterns we employ are designed to minimize overlap between simultaneously active illumination fields for uniform coverage and better signal separability. For Architecture 1, this illumination cycle yields a mixing matrix with 79,776 rows (277 illumination patterns × 288 D-pixels), thereby yielding the effective number of measurements, or effective *channels*, in each recorded sample. For linear de-mixing, the number of channels also sets the upper limit for the number of separable sources.

Operating with pulsed illumination is important for circumventing what might otherwise result in an accumulation of diffusively propagating photons that could create a obfuscating (contaminating) light background. Such considerations are especially important for architectures where many multi-shank modules are tiled to cover extended brain regions. To circumvent a diffusive (multiply scattered) light background emanating from remote modules that could potentially contaminate a given modules recording, only a single module's emitters are activated at any given time. This is feasible while still preserving rapid data acquisition because the integrated neurophotonics paradigm is so fast: the base acquisition time (~10 ns) is orders of magnitude shorter than the typical interval between action potentials (~1 ms). By temporally interleaving data acquisition from multiple modules sequentially, the background generated from an individual module's excitation light will decay before an adjacent module is queried. In this manner, essentially all the background fluorescence generated by a specific activated module will decay sufficiently to avoid light contamination in subsequent measurements within adjacent modules. For the wavelengths employed, the lifetime of the cloud of multiply scattered photons is ~7.5 ns, during which they diffuse ~2 cm. With a repetition rate of 80 MHz (12.5 ns intervals), the diffusive light contamination from one module to those adjacent to it will decay by a factor of 10^8 and thus contribute a negligible background.

Computational Modeling: Interpretation and Insights

To gain a deeper understanding of how the properties of the probe design affect the separability of signals, we decomposed the de-mixed spike SNRs into two factors: the normalized spike amplitude and the de-mixing factor. In Figure 8C, each point on the graphs represents a single fluorescent signal source (e.g., a neuronal soma), represented by its normalized spike amplitude (on the x axis) and its de-mixing factor (y axis). Normalized spike amplitude is calculated as the SNR of a single calcium spike due to one action potential, while all the other cells (sources) are kept at a fixed, average level of fluorescence. In this case, noise arises solely from the finite photon statistics. The de-mixing factor on the y axis is the cosine of the angle between the given cell's signal vector and the hyperplane formed by the activity of all other cells in the multi-dimensional signal space of all recorded channels. If a given neuron has a high normalized spike amplitude, it indicates that the cell is well positioned with respect to a small ensemble of nearby E- and D-pixels (i.e., their spatial separations are within several optical attenuation lengths). A high de-mixing factor indicates that the cell's activity produces a distinct pattern across the recorded channels and that it can effectively be de-mixed from other signals. The de-mixed SNR is the product of the normalized spike amplitude and the de-mixing factor. In Figure 8C, we provide an isoline indicating de-mixed SNR levels of 1.0 (thick diagonal red line) and two thinner, parallel red lines demarcating SNR levels of 0.3 and 3.0.

When the fluorescent source density is low (e.g., 5,000 sources/mm³; ~3,000 sources within the embedding volume in Architecture 1), about 18.5% of cells yield calcium spike SNRs, after de-mixing, in excess of 1.0 (Figure 8C). As the density of sources increases with higher-percentage somatic labeling, both factors of de-mixed spike signal quality deteriorated. First,

the normalized spike amplitude decreases because of the more intense background fluorescence from the other cells. Second, the de-mixing factor also decreases since the distinctiveness of signal distributions across all the recorded channels is reduced with densely spaced sources. In other words, with increasing labeling density, the rising intensity of background light "washes out" the desired fluorescence signals. As a result, when labeling density approaches 100% (i.e., 100,000 neurons/mm³, the typical cell density in mouse cortex), only 1.2% of all the neurons provide a SNR > 1.0 for Architecture 1, our initial and most simplistic system configuration (Figures 8C and 8d).

Architectures 2,3, and 4: Enhanced Separability

For Architecture 1, the fast drop in signal separability with labeling density arises from both the fast decrease in illumination intensity from the Lambertian sources and the lack of spatial selectivity in the emission and detection fields (given their broad and uniform intensity profiles.) These shortcomings can be addressed by enhancing spatial selectivity by making three modifications to increase what we term the *spatial diversity* of the pixels: narrowing the emission beams from the E-pixels, enabling steering of the emitted beams, and spatially modulating the angular detection selectivity of the D-pixels. Increasing the spatial diversity of both E- and D-pixels results in sharper focusing of the resulting illumination-collection fields.

The second design we present, Architecture 2, comprises 34 E-pixels and 33 D-pixels spaced uniformly along the full 1 mm active length of its 19 shanks. In this case, the shanks are arranged as an equilateral triangular lattice with 200 μm pitch (Figure 8B). The volume of tissue spanned by one module becomes 0.412 mm³; in mouse cortex, this comprises ~41,000 neurons. We assume that the E-pixels measure 10 μm × 10 μm in size and that the D-pixels measure 10 μm × 20 μm. Each pixel's field is oriented 112.5° clockwise from pixel immediately above it on the shank to form a helical pattern (Figure 8B). In this case, the beams from the E-pixels are narrowed to 60° cones. Further, the beams from the E-pixels are steerable in the shank's plane, in the direction along its length, by up to 60°. We again follow the same procedure—here with a pixel count totaling 646 E-pixels and 627 D-pixels—to design an optimized illumination cycle conveying a total optical power of 0.916 mW into the tissue. We separately integrate over signals acquired by imposing 127 distinct illumination patterns, which yields 82,042 recorded channels (127 × 646)—greatly exceeding the number of neurons within the module's target volume. The detection fields of the D-pixels were narrowed with a sensitivity profile modeled as the eighth power of the cosine of the angle between photons' incident direction and the unit vector normal to the D-pixel surface. This restriction of the D-pixel spatial sensitivity profile reduces detection efficiency by 80% as compared to the case without beam narrowing, but it nonetheless results in significant improvement in de-mixing. This second architecture produces higher de-mixed spike SNRs that persist up to much higher source labeling densities (Figures 8C and 8d), with 99.8% of cells producing single-spike SNR > 1.0 at cell labeling density of 5,000 mm⁻³. Yet with higher labeling densities, the fractions of separable cells drop again so that, at 50,000 mm⁻³ labeling density, only ~20% (or about 10,000 cells) express

de-mixed spike SNR > 1.0, and by 100,000 mm^{-3}, this fraction drops to 5%.

In Architecture 3, further narrowing the E-pixels' light emission profiles from 60° to 15° produces another sharp jump in performance approaching 95.5% de-mixing rate with spike SNR > 1.0 at 20,000 mm^{-3} labeling density and 73.1% at 50,000 mm^{-3}, only dropping to 19.3% at 100,000 mm^{-3}.

Thus, the probe design provides multiple control knobs for tuning the signal separability, including the numbers and shapes of the illumination fields and the number and shapes of the collection fields. To see what it would take to densely record a complete population, we transformed Architecture 3 into Architecture 4 by reducing the shank spacings to 150 µm (from the original 200 µm in Architecture 3), without changing other geometric properties. This reduced the recorded volume to 56.25%, but the spike SNR increased by a much greater degree, nearly 5-fold in Architecture 4, on average. Here, the number of frames in the illumination cycle was reduced to 79, producing 51,034 channels (79 × 646), with 1.47 mW of optical power being delivered into the tissue. Thus, in Architecture 4, 49.0% of cells yielded single-spike SNR > 1.0 after de-mixing at the full labeling density of 100,000 mm^{-3} (Figure 8D).

We find these results to be slightly improved when the scattering length, L_{sc}, is increased by a factor of two (i.e., from 50 up to 100 µm), whereas decreasing L_{sc} precipitously (by a factor of 1,000) reduces separability to zero, as expected.

We note again that here we measure the SNR of spikes once the optimal de-mixing matrix is obtained through a source separation method. We do not yet tackle the problem of finding the de-mixing matrix. The mathematical formalism in these simulations allows us to select optimal designs that, at least in theory, can record from dense populations. These simulations demonstrate that the geometric arrangements and shapes of the illumination and detection fields are much more effective at controlling the SNR of de-mixed signals than the illumination intensity. The analysis highlights the key advantages of integrated neurophotonics over related methods such as DOT by bringing the E-pixels and D-pixels close to the imaged tissue and shaping the fields of illumination and light collection for increased spatial selectivity. Much work remains in finding the optimal combinations of these arrangements and trade-offs against other factors such as tissue displacement.

PHOTONIC NEURAL PROBES: THE TECHNOLOGICAL BUILDING BLOCKS

The elements required to achieve the integrated neurophotonics paradigm are now being realized. Over the past 15 years, silicon integrated photonics has rapidly matured as a technology. Advances in this field now position it to engender new classes of mass-producible and widely deployable nanophotonic technologies for neuroscience. Silicon integrated photonics leverages the worldwide CMOS manufacturing infrastructure to enable fabrication of photonic devices and circuits on large-diameter silicon wafers (200 mm or 300 mm) by following well-established protocols for very large-scale integration (VLSI) of electronic devices. These technological developments are commercially driven by the continually increasing bandwidth demands for data communication and also by the increasing number of commercial and R&D scale semiconductor foundries now invested in and producing silicon photonic systems.

Although significant investment has been made worldwide to advance integrated photonics for telecommunications, the wavelengths employed by the telecom industry are in the NIR (typically >1 µm). This is unfortunate for neuroscience; it renders this extensive global technological manufacturing base largely incompatible with the requirements for addressing optogenetic actuators and molecular reporters operating at visible wavelengths. However, there are other CMOS-compatible materials beyond silicon that are transparent at visible and NIR wavelengths; these are now being carefully engineered to be compatible with the processes and protocols used in CMOS foundries. These provide the basis for visible-wavelength integrated photonic technology, which is advancing steadily but is still in its infancy. We and others are currently pursuing this avenue to enable mass-producible visible-wavelength integrated photonic and neurophotonic systems (Fowler, 2019; Jans et al., 2018; Sacher et al., 2019c). However, realizing visible-wavelength photonic devices and circuits is challenging compared with infrared photonics. Given the smaller visible wavelengths, they necessitate smaller feature sizes and much tighter control over fabrication variations and surface roughness. These challenges are now being surmounted through careful design and a succession of engineering refinements. The field of visible-wavelength integrated neurophotonics is beginning to leverage robust industrial-grade silicon integrated photonic technologies to produce miniature implantable imaging systems *en masse*. Only through use of robust and stable foundry processing can photonic components be fabricated in the requisite volume, precision, and sophistication required to meet the needs of integrated neurophotonic systems.

Passive E-Pixel Arrays

Microscale light sources typically operate only with modest efficiency; hence, they can dissipate significant power when operated. Furthermore, neural activation thresholds (Goldin and Mindlin, 2017; Moser et al., 1993; Owen et al., 2019; Thompson et al., 1985) and blood flow (Rungta et al., 2017) can be significantly altered by only small temperature changes. Accordingly, for our systems, we produce and control light "off-probe" for optogenetic actuation and chromophore excitation to preclude risk of local tissue heating. The output optical power of a single E-pixel used in our proposed architectures (20 µW, corresponding to 200 mW/mm^2) is within the range delivered by commercial optogenetic hardware (Senova et al., 2017) and induces only a modest local elevation of temperature—as confirmed by thermal imaging experiments of optical stimulation of brain tissue (Senova et al., 2017). In addition, on average, per illumination frame (2 ms) only 75 E-pixels are on simultaneously, and the same pattern of ON pixels is not repeated consecutively. Each illumination pattern has a duty cycle, roughly once every ~100 frames, which leads to an average power of 7.4 mW in a cubic millimeter of brain tissue at most (Yatsenko et al., 2020). We have already experimentally validated that our power levels (~10–100 µW per E-pixel) are non-damaging, both *in vitro* (with brain slices) and *in vivo* (in mouse) (Segev et al., 2017; Sacher et al. 2020).

The power range of 10–100 μW per E-pixel corresponds to, or is below, the typical power levels used in photostimulation of opsins. For the simulations reported here, we have kept to the low end of this range.

Our present approach for realizing implantable photonic probes E-pixel arrays thus focuses on *passive*, "on-probe" nanophotonic components. Our specific needs in this regard do not detract from the excellent advances in neurotechnology recently made with on-probe light sources. Here, we mention the significant achievement of combining LEDs and Ephys electrodes for concurrent optogenetic stimulation and electrophysiological recording (Mohanty et al., 2020; Wu et al., 2015). For our present application, however, *many hundreds* of microscale light sources are required within small tissue volumes, and this likely precludes use of active emitters, unless heavily duty-cycled operation can be employed to keep average power sufficiently low.

As mentioned, today a minority of efforts in photonics VLSI focuses on visible wavelength components. Accordingly, for this effort, we have developed a complete fabrication process for photonic components using thin-film silicon nitride (SiN). This material is transparent at visible wavelengths and is compatible with CMOS processes.

Optogenetic Simulation with Microscale Beams: First Experiments

We have demonstrated the functionality of the first photonic probe prototypes by achieving single-cell optogenetic stimulation (Segev et al., 2017). A single E-pixel photonic probe was implanted within a mouse with cortical neurons co-expressing both ChR2 and GCaMP6s. The photonic neural probe provided local, cellular-scale illumination to induce optogenetic stimulation, while neuronal activity was recorded simultaneously via free-space, 2p calcium functional imaging. The photonic probe was inserted into cortical layer 2/3 of an awake, head-fixed mouse. The probe-generated illumination beam was directed upward from the probe surface into the brain tissue, and a local population of neurons was imaged approximately 130 μm above the probe tip. The microscale beam width at the imaging plane was only ~20 μm FWHM (full width at half maximum); in other words, it is roughly of cellular dimensions. These first-generation probes have also been successfully used to achieve optogenetic manipulation of medullary neurons in the locust optic lobe (Wang et al., 2018).

Spatial Addressing of E-Pixels

To increase the number of E-pixels that can be addressed with a single wavelength, we have successfully realized a spatial addressing strategy first devised by Zorzos et al. (2012). Using a MEMS scanning mirror with ~10 ms switching times and relay optics, laser light is directed to different cores of a fiber bundle comprising thousands of micron-scale optical cores. This fiber bundle is edge-coupled to the probe chip using on-chip tapered edge couplers; this enables broadband optical coupling over the visible spectrum. Once on-chip, light is then routed by integrated photonic waveguides, delivered to grating-coupler-based E-pixels, and subsequently emitted into the tissue. We have previously employed wavelength division multiplexing (Bannerjee

et al., 2005) to allow selection of specific E-pixels by small changes in wavelength within the opsin absorption band (Fowler, 2019; Segev et al., 2015). To free wavelength control to tune another parameter (specifically, emission angle, as described next), we have employed the aforementioned MEMS-based multiplexing scheme in our most recent work.

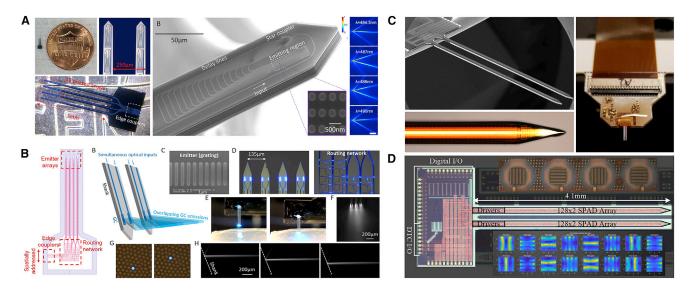### Scanning Microbeams (Coherent Beam-Forming Phased Arrays)

With the spatial addressing of E-pixels as described above, laser wavelength can be used to provide an independent degree of freedom for control. Employing this, we have developed beam-steerable E-pixels based on optical phased arrays, wherein modulation of the input wavelength results in a modulation of the output angle of the E-pixel beam (Figure 9). Again, to employ this strategy, the wavelength range used for tuning is kept within the absorption band (typically 40–50 nm wide) of the actuator and reporter chromophores we employ. When implanted in brain tissue slices, these beam-steering E-pixel probes demonstrate highly collimated, steerable beams of light emanating from grating couplers. Their successful operation in brain tissue confirms that the emitted light remains spatially coherent in brain tissue over distances of a few hundred microns, despite strong optical scattering. Our first generation of steerable E-pixel probes are comprised of four shanks, each populated with four compact, visible-wavelength phased arrays in two configurations employing: (1) a 20 nm wavelength steering range or, (2) with larger phased arrays, a 6 nm range. Future optimization can readily provide significant performance enhancements. The requisite on-probe photonic circuitry includes: a single-mode input waveguide, a star coupler to split the input light into an array of 16 waveguides, and an array of gratings on a constant sub-micron pitch to form the compound E-pixels that emit light from each of the 16 waveguides. Our use of narrow individual grating elements results in a large emission cone along the array axis and array emission interference that is complete within ~100 μm of the emitter.

These prototypes have been validated *in vitro* using adult brain slices of transgenic mice expressing a fluorescent reporter (YFP) and an opsin (ChR2). Continuous beam steering over ±14° is achieved in mouse brain slices with the capability to deliver more than 100 μW of optical power. These first-generation prototypes provide large, parallel, multi-beam illumination coverage. This will enable a multiplicity of independent illumination fields in brain tissue, as depicted in Figure 3C (Fowler, 2019; Sacher et al., 2019b).

Implantable Probes for Light-Sheet Illumination at Arbitrary Brain Depths

We have also developed implantable neural probes that generate controllable and addressable light sheets at depth for LSFM (Fowler, 2019; Sacher et al., 2019a). Figure 9B shows that these photonic neural probes deliver sheets of light parallel to the surface of the brain. The light sheets are synthesized from the emission of rows of grating couplers (GCs) that are designed to provide large emission divergences along the sheet width axis and small divergences along the sheet thickness axis. An array of input edge couplers is spatially addressed by the methods

Figure 9. Photonic Neural Probes

First-generation hardware developed for implantable probes includes emitter-pixel (E-pixel) arrays for cellular-scale patterning and delivery of visible coherent light and detector-pixel (D-pixel) arrays based upon visible spectrum, angle-selective single-photon avalanche diode (AS-SPAD) detectors.

(A) Beam-scanning E-pixel array photonic neural probes. Left: optical micrographs of neural probes with the beam-scanning E-pixels designed to operate with blue light (480 nm). Center: scanning electron micrograph (SEM) of phased array E-pixel design with ∼6 nm free spectral range (FSR). Right: top-down (steering-plane) images of the phased array emission pattern in fluorescein at multiple addressing wavelengths. Continuous scanning is possible by sweeping the input wavelength within the FSR (spectral addressing) (Sacher et al., 2019b).

(B) Light-sheet E-pixel array photonic neural probes. Left: schematic of the probe-based light patterning using the composite emission of four microscale E-pixel arrays based on grating couplers, which are fed with tightly controlled optical modes to produce addressable light sheets with ∼10–20 μm thickness. Each facet of the on-chip single-mode waveguides on the photonic probe is aligned to a core in the fiber bundle. Spatial addressing using a MEMS mirror allows temporal addressing of multiple planes and provides the requisite intensity per sheet to induce fluorescence by the one-photon excitation process. (Sacher et al., 2019a). Top right: SEM and optical micrographs of a grating, multiple grantings, and the waveguide routing network, respectively. Center right: the packaged probe before and after insertion into an agarose block and a top-down micrograph of a sheet in in fluorescein. Bottom right: edge-view micrographs of three sheets in fluorescein.

(C) Detector-pixel array (D-pixels) based upon visible spectrum angle-selective single-photon avalanche diode (SPAD) detectors: first-generation, minimally invasive photonic neural probes for lens-less functional imaging (Choi et al., 2019, 2020; Lee et al., 2019). Images of a SPAD-based D-pixel array; in clockwise order: SEM of a rectangular CMOS die post-processed into shanks, waterproof flat flexible cable (FFC) assembly used for *in vivo* insertion, and shank with an epoxy-based 10-μm-thick absorption filter coating.

(D) Micrograph of CMOS imager probe consisting of 512 SPADs along two 4-mm-long shanks. Each pixel is masked with semi-unique off-axis Talbot gratings that vary in angular direction, angular frequency, and phase (four examples shown at top), resulting in one of 16 distinct detection fields (bottom). The 16-pixel ensemble consists of two detection field directions (x-z, x-y), two angular frequencies, and four phases to minimize overlap between neighboring pixels. Pixel pitch: 25 μm × 75 μm, PDP (median): 16.8%, DCR (median): 40 Hz, time-gate resolution: 140 ps, max. frame rate: 50 kiloframes/s (Choi et al., 2019, 2020; Lee et al., 2019).

described above; they enable independent control of the multiple light sheets. Our first-generation prototypes generate five sheets that can be rapidly switched (Fowler, 2019; Sacher et al., 2019a, 2020). Working with our photonic foundry collaborator, Advanced Micro Foundry (AMF), we fabricated these probes using a 200 mm wafer-scale process. Using free-space beam profiling, average light sheet thicknesses between 10 and 15 μm were measured for sheet propagation distances between 100 and 300 μm.

Current Limitations and Developments

Critical for scale-up and mass production are robust and reproducible methods for *device packaging*. While envisioning the packaging requirements for a planar electronic chip is straightforward, for integrated neurophotonic systems, this is more complex. Here, we require a rather significant number of high-quality photonic and electronic connections to the outside world. Accordingly, new and sophisticated packaging methods must be innovated. Our present methodologies (as well as those of most other groups) are still more akin to handcraft than to bona fide engineering technology. While focus upon this area may at first glance seem rather pedestrian, development and investment of in-packaging methods for integrated photonics is *essential* for this technological paradigm to become robust, reproducible, and widely deployable. Ultimately, to achieve mass production, these packaging processes must be automated. It is worth noting that microchip technology for electronics also had to carefully address similar issues to attain mass production, robustness, and reproducibility.

Currently, a principal source of optical loss in our neurophotonic probes is the fiber-to-chip edge couplers, which exhibit coupling efficiencies of ∼15% at the 488 nm wavelength in our current work. In addition, the aperiodic spacing of the cores in the fiber image bundle coupled to the probe chips add insertion loss due to misalignment between the fiber cores and the edge couplers. By adopting more complex, multi-layer photonic integration, wherein multiple waveguide layers are vertically integrated on-chip, these optical transmission limits can be surmounted.

Following similar strategies used for silicon photonics at infrared wavelengths (Fang et al., 2010; Park et al., 2013), our simulations indicate that bilayer SiON-SiN edge couplers can achieve broadband coupling efficiencies approaching ~80%. Furthermore, integrating multiple SiN waveguide layers that can cross over one another with low optical losses and crosstalk (Sacher et al., 2017) will enable higher densities of GC emitters.

Active D-Pixel Arrays: SPADs

Concurrent with our development of integrated photonics for E-pixel arrays, we have also designed and fabricated CMOS photon-counting imaging arrays with the form factor of an implantable shank. These permit fluorescence imaging deep within brain tissue (Figure 9) (Choi et al., 2019, 2020; Lee et al., 2019). In one of our recent prototypes, a D-pixel array consists of 512 single-photon avalanche diodes (SPADs) aligned in a linear configuration that spans the length of the shank. Their field of view is to the side to maximize the ratio of observable tissue to that displaced during insertion (Rustami et al., 2020). This configuration allows the probe to monitor neurons along its length, in contrast with typical endoscopic fibers that solely image near their tips. This advance provides an order of magnitude larger field of view. Digital addressing and data readout of these pixels also makes our solution highly scalable—in this prototype, 32,768 pixels are multiplexed using only 15 parallel wires running along the shank. As mentioned, an important design goal for miniature neural probes is attainment of small cross-sectional areas to suppress immune response and avoid gliosis after implantation. Accordingly, we post process the acquired rectangular CMOS dies into 100-μm-wide, 40-μm-thick shanks, with a length of 4.1 mm. This yields an insertion cross section similar to that of a 70-μm-diameter endoscopic fiber.

To further minimize tissue displacement, we eschew the relatively thick focusing lenses typically employed for conventional microscopy. Instead, we incorporate angle-sensitive SPADs. These employ the Talbot effect, by means of CMOS metallization layers situated 3–6 μm away from the SPAD active layer. Together, they shape the angle-dependent collection fields of the photodetectors (Wang et al., 2009). This very compact solution is ideal for implantable photonic neural probe applications (Figure 9), as compared to other lens-less imagers (e.g., far-field instantiations that require a 200 μm spacer in the light path) (Adams et al., 2017). Additionally, on top of the CMOS devices, we fabricate compact single-micron-thickness spectral filters, which combine absorption and interference filters (Sasagawa et al., 2018). These provide additional spectral filtering between the bright emission pulses delivered by E-pixels and the weak, photon-limited fluorescence signals detected by D-pixels. To further suppress source-detector crosstalk, we also employ fast, time-gated pixel operation in sync with a pulsed laser driving the E-pixels, as is often used for fluorescence lifetime imaging (Ulku et al., 2019; Wang et al., 1991). Together, the absorption, interference, and time gating are employed to reject the blue light employed to excite the fluorescence of the optical reporters.

The 512-pixel SPAD array is fabricated with a 6.3% fill factor and a pixel pitch of 25.3 μm along the length of the shank (Choi et al., 2019, 2020; Lee et al., 2019). Each D-pixel provides a photon detection probability (PDP) larger than 10% in the visible fluorescent spectral band of most biomarkers (500–600 nm), with a median dark count rate of 40 counts per second (cps) at room temperature. The power dissipated on the shank is dominated by the charging of the SPAD capacitance at quenching events, consuming a total of 97 μW under dark conditions and 68 mW in full-output saturation lighting. There is much headroom for further optimization; 2D SPAD arrays have recently been demonstrated with a pixel pitch as small as 2.2 μm (Morimoto and Charbon, 2020), 61% native fill factor (Gyongy et al., 2018). Today's state-of-the-art 3D integration techniques will enable even higher fill factors to be attained.

Each pixel is masked with two layers of parallel Talbot gratings to create an angle-dependent field of view. Different combinations of angular modulation direction (x, y), frequency (β = 12, 20), and phase (α = 0°, 90°, 180°, 270°) give rise to 16 uniquely shaped collection fields, which are overlaid upon the 512-pixel array (Wang et al., 2009). We employ the combined information from these collection fields to increase the spatial selectivity of our system, and this greatly enhances the effectiveness of computational procedure we employ to attain source separation.

The post-processed imaging shank, wire-bonded and packaged to be waterproof, links to a field-programmable gate array (FPGA) chip through a 51-wire flat flexible cable. On the FPGA, a microcontroller, state machine, and data-FIFO control the photon collection and frame readout with a maximum rate of 50 kfps (i.e., 20 μs per frame). This rate can be readily increased in future generations. The time-gate filter, implemented as a phase-locked loop (PLL) on the FPGA, can be fine-tuned with a resolution of 140 ps for optimal signal collection. The FPGA then links to a computer through a USB-3 link that displays a real-time representation of photon counts in 3D volume (Choi et al., 2019). To illustrate the speed of our D-pixel imagers, we have recently demonstrated nanosecond-scale fluorescence imaging a standard fluorophore with one of these shanks (Choi et al., 2019; Lee et al., 2019). Accordingly, tracking the fastest of today's voltage reporters is assured.

Co-Integration of D- and E-Pixel Arrays

Ultimately, photonic neural probe-array architectures must provide not only dense tissue coverage but must also be produced by a cost-effective strategy that enables co-integration of their many electronic and photonic subcomponents. We foresee four potential phases of technological evolution in this regard. Initially, multi-shank imaging "modules" will be straightforwardly assembled from separate E-pixel and D-pixel probe layers that are first thinned and then subsequently stacked back-to-back individually.

As mentioned above, optimal consolidation of all the separate microscale imaging components for mass production must eschew piecemeal assembly; instead, true wafer-scale co-integration will be required. This must ultimately be achieved at the foundry by heterogeneous (multiple materials) process integration. In the simplest, second phase, the photonic and electronic devices can be separately integrated and subsequently conjoined by wafer-scale bonding. In this case, the photonics layer will include openings to provide access for the underlying D-pixels to clear, photon-collection-path *vias*. This will enable

functionality from both the front and back of the shanks. A third, more complex approach will involve wafer-scale production of the photonics layers in post process—that is, *after* the wafers containing the CMOS imagers are foundry fabricated. This will be executed directly upon the electronics wafer containing the D-pixel arrays and their associated circuitry. The fabrication process must make use of low-temperature SiN processes to avoid compromising the performance of the CMOS imaging elements; PECVD SiN with a 300°C deposition temperature will be employed. Such processing is compatible with CMOS circuits, and the material provides sufficiently low absorption at visible wavelengths (Gorin et al., 2008; Sriram et al., 1983). More recently, even lower-temperature (75°C) SiN processes show sufficiently low infrared losses that may translate to the visible (Shao et al., 2016). In an ultimate fourth phase, where production is advanced to cost-effective, large-scale manufacturing, 3D integration of separately processed photonics and electronics layers will be employed. This is the most advanced solution with significant upfront costs, but it will provide the highest level of dimensional accuracy, integration density, and device complexity—and, ultimately, enable the lowest per-unit costs once initial engineering expenses are invested. Our approach to this complex undertaking involves the previous three phases; by proceeding through the first three intermediate steps, we will ensure success of this final, and most complex, undertaking.

CONCLUSIONS AND PROJECTIONS

The Integrated Neurophotonics Paradigm: Status Quo

Over the past several years, we have achieved many significant milestones that advance us toward attaining full realization of this exciting, albeit complex, paradigm of integrated neurophotonics. We have developed reliable and low-loss wafer-scale mass-production processes for visible-wavelength integrated nanophotonics by working with our foundry partners. With this in place, we have made significant advances, including: demonstration of coherent optical beam formation within brain tissue; realization of beam-steerable phased arrays of micro-emitters (E-pixels) and selective-plane (light-sheet) illumination with implantable E-pixel probe arrays; and creation of implantable, angle-selective single-photon microdetector (D-pixel) arrays. These constitute the fundamental building blocks for complete implantable visible-wavelength functional imaging systems with microscale dimensions. Further, we have validated the foundational physics for the integrated photonics paradigm by developing and implementing computational methods to evaluate the fluorescent photon yield in scattering media. This has elucidated the regime of mesoscopic light scattering, in which ensembles of closely spaced microscale imaging components—and the integrated neurophotonics paradigm—operate. We have also developed a mathematical formalism and a framework for numerical simulations to compare and optimize the expected signal quality for various system architectures. The ultimate metric for performance is signal separability, and we have explored this as a function of increasing optogenetic labeling density (from sparse to dense). With these tools, we have validated our computational approach for optical source separation and localization and, thereby, have been able to identify practical, *realizable* architectures that can enable dense volumetric activity reconstruction at depth.

Together, these developments validate the potential of the integrated neurophotonics paradigm for achieving fast, dense, and deep functional imaging in brain tissue. This new technological approach has promise to surmount the limitations of existing methodologies. It is being developed to enable: (1) optically based electrophysiological recording and stimulation in real time—with cellular resolution, in all regions of the brain, no matter how deep; (2) dense coverage of neuronal populations within large target volumes; and (3) cell-specific interrogation (via targeted optogenetic actuators and molecular reporters) permitting complex and finely tuned activity control. Finally, these systems are based on mass-production processes routinely carried out in existing electronic- and photonic-chip foundries. The ultimate prospect of wide dissemination of complete measurement systems to the neuroscience community, given requisite support, is thus assured.

What Is the Requisite Technological "Basis" for Mapping Brain Circuits?

A scientific debate emerged in conjunction with the launch of the US BRAIN Initiative concerning the optimal path forward for unraveling fundamental mechanisms, or *computational motifs*, that underlie brain function. Identifying a specific and sufficiently complete "basis set" of experimental measurements to enable such elucidation is essential. Knowledge of this basis will, in turn, enable us to identify the requisite neurotechnologies to acquire such data. A prevalent view is that connectomics and large-scale measurements of brain activity—among the most widely applied of modern approaches that provide anatomical and functional maps, respectively—are both complementary and necessary. But it has also asserted that even this combined approach will likely ultimately prove insufficient. The quest is further complicated by the fact that brain circuits employ other physicochemical *activity domains* for control (Figure 1B), among which are dynamical alteration of neurons and circuits through spatiotemporal neuromodulation of channels, synapses, and local biochemistry. And compounding the complexity of this measurement challenge is the immense variety of distinct cell types encompassed within brain circuits, each of which can carry out unique, complementary, and coherent functions through interactions with others.

With this perspective, it seems that the requisite technological basis for mapping brain circuitry will ultimately likely include:

1. acquiring knowledge of anatomical connections (connectomics),
2. assessing synaptic connection strengths,
3. monitoring localized electrophysiological activity on a massively parallel scale,
4. precisely stimulating neural activity at the cellular, if not synaptic, level (i.e., circuit "interrogation"),
5. identifying the individual cell types that participate, and,
6. observing, simultaneously, the spatiotemporal dynamics within multiple activity domains, among which include the biochemical (for neuromodulation, as mentioned) and the mechanical (to assess biological forces that arise, for example, in synaptogenesis).

Beyond Spiking

We especially wish to highlight the last point (6). The necessity of acquiring real-time *multi-physical* data, *simultaneously*, from a multiplicity of measurement domains underscores the need for new hardware (and associated software) for brain activity mapping that profoundly transcends present-day capabilities. Further, by multiplexing the emission and excitation wavelengths of the chromophores comprised within molecular reporters, and assembling multi-color integrated neurophotonic systems to interrogate them, activity from different domains (Figure 1B) can be simultaneously monitored (Cohen et al., 2018). This will enable the much more comprehensive multi-physical mapping of brain activity we envisage. As we have emphasized, integrated neurophotonics can be readily adapted for such investigations.

Projections

The convergence of these new technologies—optogenetic actuators and reporters of brain activity with specificity of cell type and mass-manufacturable photonic and electronic integrated circuitry enabling microscale implantable systems—now provide an unprecedented opportunity to realize a new class of multi-physical functional imaging tools for neuroscience. We anticipate that these powerful tools will transform brain activity mapping, will enable new types of closed-loop brain interfaces with unparalleled recording capabilities, and will enable a powerful paradigm for multi-physical interrogation of the brain activity with spatial and temporal resolutions that cannot be attained by existing methodologies.

DECLARATION OF INTERESTS

Three patents owned by the California Institute of Technology have been pursued in connection with this work: (1) Roukes (2011). Brain-machine interface based on photonic neural probe arrays. U.S.P.T.O. Patent No. 10,638,933, Issued May 5, 2020, Priority Date: December 8, 2011. (2) Segev, E., Moreaux, L.C., Fowler, T.M. Faraon, A., Roukes, M.L. Implantable, highly collimated light-emitters for biological applications. U.S.P.T.O. Patent No. 10,471,273, Issue date: 12 November 2019; Priority date: 16 October 2015. (3) Roukes et al. (2016). One-photon integrated neurophotonic systems. U.S.P.T.O. Patent Application 20160150963, Filing date: November 5, 2014; Publication date: June 2, 2016.

REFERENCES

Acher, F.C., and Bertrand, H.O. (2005). Amino acid recognition by Venus flytrap domains is encoded in an 8-residue motif. Biopolymers 80, 357–366.

Adams, J.K., Boominathan, V., Avants, B.W., Vercosa, D.G., Ye, F., Baraniuk, R.G., Robinson, J.T., and Veeraraghavan, A. (2017). Single-frame 3D fluorescence microscopy with ultraminiature lensless FlatScope. Sci. Adv. 3, e1701548.

Adrian, E.D. (1926). The impulses produced by sensory nerve endings: Part I. J. Physiol. 61, 49–72.

Ahrens, M.B., Orger, M.B., Robson, D.N., Li, J.M., and Keller, P.J. (2013). Whole-brain functional imaging at cellular resolution using light-sheet microscopy. Nat. Methods 10, 413–420.

Alivisatos, A.P., Chun, M., Church, G.M., Greenspan, R.J., Roukes, M.L., and Yuste, R. (2012). The brain activity map project and the challenge of functional connectomics. Neuron 74, 970–974.

Andreoni, A., Davis, C.M.O., and Tian, L. (2019). Measuring Brain Chemistry Using Genetically Encoded Fluorescent Sensors. Curr. Opin. Biomed. Eng. 12, 59–67.

Azizi, L., Zarychta, K., Ettori, D., Tinet, E., and Tualle, J.-M. (2009). Ultimate spatial resolution with Diffuse Optical Tomography. Opt. Express 17, 12132–12144.

Bannerjee, A., Park, Y., Clarke, F., Song, H., Yang, S., Kramer, G., Kim, K., and Mukherjee, B. (2005). Wavelength-division-multiplexed passive optical network (WDM-PON) technologies for broadband access: a review. J. Opt. Networking 4, 737–758.

Bargmann, C., and Newsome, W. (2014). BRAIN 2025: A Scientific Vision (Advisory Committee to the Director, NIH).

Beaulieu, D.R., Davison, I.G., Kılıç, K., Bifano, T.G., and Mertz, J. (2020). Simultaneous multiplane imaging with reverberation two-photon microscopy. Nat. Methods 17, 283–286.

Berényi, A., Somogyvári, Z., Nagy, A.J., Roux, L., Long, J.D., Fujisawa, S., Stark, E., Leonardo, A., Harris, T.D., and Buzsáki, G. (2014). Large-scale, high-density (up to 512 channels) recording of local circuits in behaving animals. J. Neurophysiol. 111, 1132–1149.

Bohren, C.F., and Huffman, D.R. (2004). Absorption and Scattering of Light by Small Particles (Wiley-VCH Verlag GmbH & Co. KGaA).

Bouchard, M.B., Voleti, V., Mendes, C.S., Lacefield, C., Grueber, W.B., Mann, R.S., Bruno, R.M., and Hillman, E.M. (2015). Swept confocally-aligned planar excitation (SCAPE) microscopy for high speed volumetric imaging of behaving organisms. Nat. Photonics 9, 113–119.

Boyden, E.S. (2011). A history of optogenetics: the development of tools for controlling brain circuits with light. F1000 Biol. Rep. 3, 11.
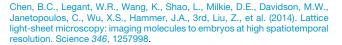
Buzsáki, G. (2004). Large-scale recording of neuronal ensembles. Nat. Neurosci. 7, 446–451.

Buzsáki, G., Anastassiou, C.A., and Koch, C. (2012). The origin of extracellular fields and currents–EEG, ECoG, LFP and spikes. Nat. Rev. Neurosci. 13, 407–420.

Campbell, P.K., Jones, K.E., Huber, R.J., Horch, K.W., and Normann, R.A. (1991). A silicon-based, three-dimensional neural interface: manufacturing processes for an intracortical electrode array. IEEE Trans. Biomed. Eng. 38, 758–768.

Charpak, S., Mertz, J., Beaurepaire, E., Moreaux, L., and Delaney, K. (2001). Odor-evoked calcium signals in dendrites of rat mitral cells. Proc. Natl. Acad. Sci. USA 98, 1230–1234.

Chen, T.W., Wardill, T.J., Sun, Y., Pulver, S.R., Renninger, S.L., Baohan, A., Schreiter, E.R., Kerr, R.A., Orger, M.B., Jayaraman, V., et al. (2013). Ultrasensitive fluorescent proteins for imaging neuronal activity. Nature 499, 295–300.

Chen, B.C., Legant, W.R., Wang, K., Shao, L., Milkie, D.E., Davidson, M.W., Janetopoulos, C., Wu, X.S., Hammer, J.A., 3rd, Liu, Z., et al. (2014). Lattice light-sheet microscopy: imaging molecules to embryos at high spatiotemporal resolution. Science *346*, 1257998.

Chen, X., Mu, Y., Hu, Y., Kuan, A.T., Nikitchenko, M., Randlett, O., Chen, A.B., Gavornik, J.P., Sompolinsky, H., Engert, F., and Ahrens, M.B. (2018). Brain-wide Organization of Neuronal Activity and Convergent Sensorimotor Transformations in Larval Zebrafish. Neuron *100*, 876–890.e5.

Chen, Y., Jang, H., Spratt, P.W.E., Kosar, S., Taylor, D.E., Essner, R.A., Bai, L., Leib, D.E., Kuo, T.W., Lin, Y.C., et al. (2020). Soma-Targeted Imaging of Neural Circuits by Ribosome Tethering. Neuron *107*, 454–469.e6.

Cheng, A., Gonçalves, J.T., Golshani, P., Arisaka, K., and Portera-Cailliau, C. (2011). Simultaneous two-photon calcium imaging at different depths with spatiotemporal multiplexing. Nat. Methods *8*, 139–142.

Choi, J., Taal, A.J., Pollmann, E.H., Lee, C., Kim, K., Moreaux, L.C., Roukes, M.L., and Shepard, K.L. (2019). A 512-Pixel, 51-kHz-Frame-Rate, Dual-Shank, Lens-less, Filter-less Single Photon Avalanche Diode CMOS Neural Imaging Probe. IEEE J. Solid-State Circuits *54*, 2957–2968.

Choi, J., Taal, A.J., Meng, W.L., Pollmann, E.H., Stanton, J.W., Lee, C., Moazeni, S., Moreaux, L.C., Roukes, M.L., and Shepard, K.L. (2020). Fully Integrated Time-Gated 3D Fluorescence Imager for Deep Neural Imaging. IEEE Trans. Biomed. Circuits Syst. *14*, 636–645.

Cohen, S., Valm, A.M., and Lippincott-Schwartz, J. (2018). Multispectral Live-Cell Imaging. Curr. Protoc. Cell Biol. *79*, e46.

Comon, P., and Jutten, C. (2010). Handbook of Blind Source Separation: Independent Component Analysis and Applications (Academic Press).

Corder, G., Ahanonu, B., Grewe, B.F., Wang, D., Schnitzer, M.J., and Scherrer, G. (2019). An amygdalar neural ensemble that encodes the unpleasantness of pain. Science *363*, 276–281.

Cotton, R.J., Froudarakis, E., Storer, P., Saggau, P., and Tolias, A.S. (2013). Three-dimensional mapping of microcircuit correlation structure. Front. Neural Circuits *7*, 151.

Daigle, T.L., Madisen, L., Hage, T.A., Valley, M.T., Knoblich, U., Larsen, R.S., Takeno, M.M., Huang, L., Gu, H., Larsen, R., et al. (2018). A Suite of Transgenic Driver and Reporter Mouse Lines with Enhanced Brain-Cell-Type Targeting and Functionality. Cell *174*, 465–480.e22.

Dana, H., Sun, Y., Mohar, B., Hulse, B.K., Kerlin, A.M., Hasseman, J.P., Tsegaye, G., Tsang, A., Wong, A., Patel, R., et al. (2019). High-performance calcium sensors for imaging activity in neuronal populations and microcompartments. Nat. Methods *16*, 649–657.

de Groot, A., van den Boom, B.J., van Genderen, R.M., Coppens, J., van Veldhuijzen, J., Bos, J., Hoedemaker, H., Negrello, M., Willuhn, I., De Zeeuw, C.I., and Hoogland, T.M. (2020). NINscope, a versatile miniscope for multi-region circuit investigations. eLife *9*, e49987.

Dehghani, H., White, B.R., Zeff, B.W., and Culver, J.P. (2008). Depth sensitivity analysis of high-density imaging arrays for mapping brain function with diffuse optical tomography. In Biomedical Optics (Optical Society of America), BMD27.

Denk, W., Strickler, J.H., and Webb, W.W. (1990). Two-photon laser scanning fluorescence microscopy. Science *248*, 73–76.

Ding, R., Liao, X., Li, J., Zhang, J., Wang, M., Guang, Y., Qin, H., Li, X., Zhang, K., Liang, S., et al. (2017). Targeted Patching and Dendritic Ca^{2+} Imaging in Nonhuman Primate Brain in vivo. Sci. Rep. *7*, 2873.

Ducros, M., Goulam Houssen, Y., Bradley, J., de Sars, V., and Charpak, S. (2013). Encoded multisite two-photon microscopy. Proc. Natl. Acad. Sci. USA *110*, 13138–13143.

Emara, M.S., Pisanello, M., Sileo, L., De Vittorio, M., and Pisanello, F. (2019). A Wireless Head-Mountable Device with Tapered Optical Fiber-Coupled Laser Diode for Light Delivery in Deep Brain Regions. IEEE Trans. Biomed. Eng. *66*, 1996–2009.

Engelbrecht, C.J., Voigt, F., and Helmchen, F. (2010). Miniaturized selective plane illumination microscopy for high-contrast in vivo fluorescence imaging. Opt. Lett. *35*, 1413–1415.

Fang, Q., Liow, T.Y., Song, J.F., Tan, C.W., Yu, M.B., Lo, G.Q., and Kwong, D.L. (2010). Suspended optical fiber-to-waveguide mode size converter for silicon photonics. Opt. Express *18*, 7763–7769.

Felder, C.B., Graul, R.C., Lee, A.Y., Merkle, H.P., and Sadee, W. (1999). The Venus flytrap of periplasmic binding proteins: an ancient protein module present in multiple drug receptors. AAPS PharmSci *1*, E2, https://doi.org/10.1208/ps010202.

Fowler, T.M. (2019). Silicon Neural Probes for Stimulation of Neurons and the Excitation and Detection of Proteins in the Brain. Dissertation (PhD) (California Institute of Technology).

Gerstein, G.L., and Clark, W.A. (1964). Simultaneous Studies of Firing Patterns in Several Neurons. Science *143*, 1325–1327.

Ghosh, K.K., Burns, L.D., Cocker, E.D., Nimmerjahn, A., Ziv, Y., Gamal, A.E., and Schnitzer, M.J. (2011). Miniaturized integration of a fluorescence microscope. Nat. Methods *8*, 871–878.

Girkin, J.M., Poland, S., and Wright, A.J. (2009). Adaptive optics for deeper imaging of biological samples. Curr. Opin. Biotechnol. *20*, 106–110.

Goldin, M.A., and Mindlin, G.B. (2017). Temperature manipulation of neuronal dynamics in a forebrain motor control nucleus. PLoS Comput. Biol. *13*, e1005699.

Gong, Y., Huang, C., Li, J.Z., Grewe, B.F., Zhang, Y., Eismann, S., and Schnitzer, M.J. (2015). High-speed recording of neural spikes in awake mice and flies with a fluorescent voltage sensor. Science *350*, 1361–1366.

Gorin, A., Jaouad, A., Grondin, E., Aimez, V., and Charette, P. (2008). Fabrication of silicon nitride waveguides for visible-light using PECVD: a study of the effect of plasma frequency on optical properties. Opt. Express *16*, 13509–13516.

Gray, C.M., Maldonado, P.E., Wilson, M., and McNaughton, B. (1995). Tetrodes markedly improve the reliability and yield of multiple single-unit isolation from multi-unit recordings in cat striate cortex. J. Neurosci. Methods *63*, 43–54.

Grewe, B.F., Langer, D., Kasper, H., Kampa, B.M., and Helmchen, F. (2010). High-speed in vivo calcium imaging reveals neuronal network activity with near-millisecond precision. Nat. Methods *7*, 399–405.

Grienberger, C., and Konnerth, A. (2012). Imaging calcium in neurons. Neuron *73*, 862–885.

Gyongy, I., Calder, N., Davies, A., Dutton, N.A.W., Duncan, R.R., Rickman, C., Dalgarno, P., and Henderson, R.K. (2018). A 256×256, 100-kfps, 61% Fill-Factor SPAD Image Sensor for Time-Resolved Microscopy Applications. IEEE Transactions on Electron Devices *65*, 547–554.

Hamill, O.P., Marty, A., Neher, E., Sakmann, B., and Sigworth, F.J. (1981). Improved patch-clamp techniques for high-resolution current recording from cells and cell-free membrane patches. Pflugers Arch. *391*, 85–100.

Haslehurst, P., Yang, Z., Dholakia, K., and Emptage, N. (2018). Fast volume-scanning light sheet microscopy reveals transient neuronal events. Biomed. Opt. Express *9*, 2154–2167.

Herreras, O. (2016). Local Field Potentials: Myths and Misunderstandings. Front. Neural Circuits *10*, 101.

Hillman, E.M.C., Voleti, V., Li, W., and Yu, H. (2019). Light-Sheet Microscopy in Neuroscience. Annu. Rev. Neurosci. *42*, 295–313.

Hoogerwerf, A.C., and Wise, K.D. (1994). A three-dimensional microelectrode array for chronic neural recording. IEEE Trans. Biomed. Eng. *41*, 1136–1146.

Horton, N.G., Wang, K., Kobat, D., Clark, C.G., Wise, F.W., Schaffer, C.B., and Xu, C. (2013). In vivo three-photon microscopy of subcortical structures within an intact mouse brain. Nat. Photonics *7*, 205–209.

Huisken, J., Swoger, J., Del Bene, F., Wittbrodt, J., and Stelzer, E.H. (2004). Optical sectioning deep inside live embryos by selective plane illumination microscopy. Science *305*, 1007–1009.

Hulse, B.K., Moreaux, L.C., Lubenov, E.V., and Siapas, A.G. (2016). Membrane Potential Dynamics of CA1 Pyramidal Neurons during Hippocampal Ripples in Awake Mice. Neuron *89*, 800–813.

Jacob, A.D., Ramsaran, A.I., Mocle, A.J., Tran, L.M., Yan, C., Frankland, P.W., and Josselyn, S.A. (2018). A Compact Head-Mounted Endoscope for In Vivo Calcium Imaging in Freely Behaving Mice. Curr. Protoc. Neurosci. *84*, e51.

Jans, H., O'Brien, P., Artundo, I., Porcel, M.A.G., Hoofman, R., Geuzebroek, D., Dumon, P., van der Vliet, M., Witzens, J., Bourguignon, E., et al. (2018). Integrated bio-photonics to revolutionize health care enabled through PIX4life and PIXAPP. In Proceedings Volume 10506, Nanoscale Imaging, Sensing, and Actuation for Biomedical Applications XV (SPIE), 105060V.

Jeong, J.W., Shin, G., Park, S.I., Yu, K.J., Xu, L., and Rogers, J.A. (2015). Soft materials in neuroengineering for hard problems in neuroscience. Neuron *86*, 175–186.

Jiang, X., Wang, G., Lee, A.J., Stornetta, R.L., and Zhu, J.J. (2013). The organization of two new cortical interneuronal circuits. Nat. Neurosci. *16*, 210–218.

Jiang, X., Shen, S., Cadwell, C.R., Berens, P., Sinz, F., Ecker, A.S., Patel, S., and Tolias, A.S. (2015). Principles of connectivity among morphologically defined cell types in adult neocortex. Science *350*, aac9462.

Jun, J.J., Steinmetz, N.A., Siegle, J.H., Denman, D.J., Bauza, M., Barbarits, B., Lee, A.K., Anastassiou, C.A., Andrei, A., Aydın, Ç., et al. (2017). Fully integrated silicon probes for high-density recording of neural activity. Nature *551*, 232–236.

Katona, G., Szalay, G., Maák, P., Kaszás, A., Veress, M., Hillier, D., Chiovini, B., Vizi, E.S., Roska, B., and Rózsa, B. (2012). Fast two-photon in vivo imaging with three-dimensional random-access scanning in large tissue volumes. Nat. Methods *9*, 201–208.

Keller, P.J., and Ahrens, M.B. (2015). Visualizing whole-brain activity and development at the single-cell level using light-sheet microscopy. Neuron *85*, 462–483.

Keller, P.J., Schmidt, A.D., Wittbrodt, J., and Stelzer, E.H. (2008). Reconstruction of zebrafish early embryonic development by scanned light sheet microscopy. Science *322*, 1065–1069.

Kleinfeld, D., Luan, L., Mitra, P.P., Robinson, J.T., Sarpeshkar, R., Shepard, K., Xie, C., and Harris, T.D. (2019). Can One Concurrently Record Electrical Spikes from Every Neuron in a Mammalian Brain? Neuron *103*, 1005–1015.

Kodandaramaiah, S.B., Franzesi, G.T., Chow, B.Y., Boyden, E.S., and Forest, C.R. (2012). Automated whole-cell patch-clamp electrophysiology of neurons in vivo. Nat. Methods *9*, 585–587.

Kothapalli, S.-R., Sakadžić, S., Kim, C., and Wang, L.V. (2007). Imaging optically scattering objects with ultrasound-modulated optical tomography. Opt. Lett. *32*, 2351–2353.

Laven, P. (2020) MiePlot: A computer program for scattering of light from a sphere using Mie theory & the Debye Series, www.philiplaven.com/mieplot.htm; Accessed 5 October 2020.

Lecoq, J., Orlova, N., and Grewe, B.F. (2019). Wide. Fast. Deep: Recent Advances in Multiphoton Microscopy of *In Vivo* Neuronal Activity. J. Neurosci. *39*, 9042–9052.

Lee, C., Taal, A.J., Choi, J., Kim, K., Tien, K., Moreaux, L.M., Roukes, M.L., and Shepard, K.L. (2019). A 512-Pixel 3kHz-frame-rate dual-shank lensless filterless single-photon-avalanche-diode CMOS neural imaging probe. In 2019 IEEE International Solid-State Circuits Conference (ISSCC), pp. 198–200.

Leopold, A.V., Shcherbakova, D.M., and Verkhusha, V.V. (2019). Fluorescent Biosensors for Neurotransmission and Neuromodulation: Engineering and Applications. Front. Cell. Neurosci. *13*, 474.

Liberti, W.A., Perkins, L.N., Leman, D.P., and Gardner, T.J. (2017). An open source, wireless capable miniature microscope system. J. Neural Eng. *14*, 045001.

Lin, M.Z., and Schnitzer, M.J. (2016). Genetically encoded indicators of neuronal activity. Nat. Neurosci. *19*, 1142–1153.

Liu, W.-W., and Li, P.-C. (2020). Photoacoustic imaging of cells in a three-dimensional microenvironment. J. Biomed. Sci. *27*, 3.

Liu, J., Fu, T.M., Cheng, Z., Hong, G., Zhou, T., Jin, L., Duvvuri, M., Jiang, Z., Kruskal, P., Xie, C., et al. (2015). Syringe-injectable electronics. Nat. Nanotechnol. *10*, 629–636.

Lu, R., Liang, Y., Meng, G., Zhou, P., Svoboda, K., Paninski, L., and Ji, N. (2020). Rapid mesoscale volumetric imaging of neural activity with synaptic resolution. Nat. Methods *17*, 291–294.

Ludwig, K.A., Langhals, N.B., Joseph, M.D., Richardson-Burns, S.M., Hendricks, J.L., and Kipke, D.R. (2011). Poly(3,4-ethylenedioxythiophene) (PEDOT) polymer coatings facilitate smaller neural recording electrodes. J. Neural Eng. *8*, 014001.

Luo, L., Callaway, E.M., and Svoboda, K. (2018). Genetic Dissection of Neural Circuits: A Decade of Progress. Neuron *98*, 256–281.

Marblestone, A.H., Zamft, B.M., Maguire, Y.G., Shapiro, M.G., Cybulski, T.R., Glaser, J.I., Amodei, D., Stranges, P.B., Kalhor, R., Dalrymple, D.A., et al. (2013). Physical principles for scalable neural recording. Front. Comput. Neurosci. *7*, 137.

Marvin, J.S., Scholl, B., Wilson, D.E., Podgorski, K., Kazemipour, A., Müller, J.A., Schoch, S., Quiroz, F.J.U., Rebola, N., Bao, H., et al. (2018). Stability, affinity, and chromatic variants of the glutamate sensor iGluSnFR. Nat. Methods *15*, 936–939.

Marvin, J.S., Shimoda, Y., Magloire, V., Leite, M., Kawashima, T., Jensen, T.P., Kolb, I., Knott, E.L., Novak, O., Podgorski, K., et al. (2019). A genetically encoded fluorescent sensor for in vivo imaging of GABA. Nat. Methods *16*, 763–770.

McNaughton, B.L., O'Keefe, J., and Barnes, C.A. (1983). The stereotrode: a new technique for simultaneous isolation of several single units in the central nervous system from multiple unit records. J. Neurosci. Methods *8*, 391–397.

Mertz, J. (2011). Optical sectioning microscopy with planar or structured illumination. Nat. Methods *8*, 811–819.

Miesenböck, G. (2011). Optogenetic control of cells and circuits. Annu. Rev. Cell Dev. Biol. *27*, 731–758.

Mittmann, W., Wallace, D.J., Czubayko, U., Herb, J.T., Schaefer, A.T., Looger, L.L., Denk, W., and Kerr, J.N. (2011). Two-photon calcium imaging of evoked activity from L5 somatosensory neurons in vivo. Nat. Neurosci. *14*, 1089–1093.

Mohanty, A., Li, Q., Tadayon, M.A., Roberts, S.P., Bhatt, G.R., Shim, E., Ji, X., Cardenas, J., Miller, S.A., Kepecs, A., and Lipson, M. (2020). Reconfigurable nanophotonic silicon probes for sub-millisecond deep-brain optical stimulation. Nat. Biomed. Eng. *4*, 223–231.

Moreaux, L., and Laurent, G. (2007). Estimating firing rates from calcium signals in locust projection neurons in vivo. Front. Neural Circuits *1*, 2.

Moreaux, L., and Laurent, G. (2008). A simple method to reconstruct firing rates from dendritic calcium signals. Front. Neurosci. *2*, 176–185.

Morimoto, K., and Charbon, E. (2020). High fill-factor miniaturized SPAD arrays with a guard-ring-sharing technique. Opt. Express *28*, 13068–13080.

Moser, E., Mathiesen, I., and Andersen, P. (1993). Association between brain temperature and dentate field potentials in exploring and swimming rats. Science *259*, 1324–1326.

Mukamel, E.A., Nimmerjahn, A., and Schnitzer, M.J. (2009). Automated analysis of cellular signals from large-scale calcium imaging data. Neuron *63*, 747–760.

Musk, E.; Neuralink (2019). An integrated brain-machine interface platform with thousands of channels. J. Med. Internet Res. *21*, e16194.

Najafi, K., Ji, J., and Wise, K.D. (1990). Scaling limitations of silicon multichannel recording probes. IEEE Trans. Biomed. Eng. *37*, 1–11.

Navaraj, W.T., Gupta, S., Lorenzelli, L., and Dahiya, R. (2018). Wafer Scale Transfer of Ultrathin Silicon Chips on Flexible Substrates for High Performance Bendable Systems. Adv. Electron. Mater. *4*, 1700277.

O'Hara, P.J., Sheppard, P.O., Thøgersen, H., Venezia, D., Haldeman, B.A., McGrane, V., Houamed, K.M., Thomsen, C., Gilbert, T.L., and Mulvihill, E.R. (1993). The ligand-binding domain in metabotropic glutamate receptors is related to bacterial periplasmic binding proteins. Neuron *11*, 41–52.

Oe, Y., Wang, X., Patriarchi, T., Konno, A., Ozawa, K., Yahagi, K., Hirai, H., Tsuboi, T., Kitaguchi, T., Tian, L., et al. (2020). Distinct temporal integration of noradrenaline signaling by astrocytic second messengers during vigilance. Nat. Commun. *11*, 471.

Oheim, M., Beaurepaire, E., Chaigneau, E., Mertz, J., and Charpak, S. (2001). Two-photon microscopy in brain tissue: parameters influencing the imaging depth. J. Neurosci. Methods *111*, 29–37.

Ouzounov, D.G., Wang, T., Wang, M., Feng, D.D., Horton, N.G., Cruz-Hernández, J.C., Cheng, Y.T., Reimer, J., Tolias, A.S., Nishimura, N., and Xu, C. (2017). In vivo three-photon imaging of activity of GCaMP6-labeled neurons deep in intact mouse brain. Nat. Methods *14*, 388–390.

Owen, S.F., Liu, M.H., and Kreitzer, A.C. (2019). Thermal constraints on in vivo optogenetic manipulations. Nat. Neurosci. *22*, 1061–1065.

Painchaud, Y., Mailloux, A., Morin, M., Verreault, S., and Beaudry, P. (1999). Time-domain optical imaging: discrimination between scattering and absorption. Appl. Opt. *38*, 3686–3693.

Park, H., Kim, S., Park, J., Joo, J., and Kim, G. (2013). A fiber-to-chip coupler based on Si/SiON cascaded tapers for Si photonic chips. Opt. Express *21*, 29313–29319.

Patriarchi, T., Cho, J.R., Merten, K., Howe, M.W., Marley, A., Xiong, W.H., Folk, R.W., Broussard, G.J., Liang, R., Jang, M.J., et al. (2018). Ultrafast neuronal imaging of dopamine dynamics with designed genetically encoded sensors. Science *360*, eaat4422.

Perin, R., Berger, T.K., and Markram, H. (2011). A synaptic organizing principle for cortical neuronal groups. Proc. Natl. Acad. Sci. USA *108*, 5419–5424.

Piatkevich, K.D., Bensussen, S., Tseng, H.A., Shroff, S.N., Lopez-Huerta, V.G., Park, D., Jung, E.E., Shemesh, O.A., Straub, C., Gritton, H.J., et al. (2019). Population imaging of neural activity in awake behaving mice. Nature *574*, 413–417.

Pisanello, F., Sileo, L., Oldenburg, I.A., Pisanello, M., Martiradonna, L., Assad, J.A., Sabatini, B.L., and De Vittorio, M. (2014). Multipoint-emitting optical fibers for spatially addressable in vivo optogenetics. Neuron *82*, 1245–1254.

Pisanello, F., Mandelbaum, G., Pisanello, M., Oldenburg, I.A., Sileo, L., Markowitz, J.E., Peterson, R.E., Della Patria, A., Haynes, T.M., Emara, M.S., et al. (2017). Dynamic illumination of spatially restricted or large brain volumes via a single tapered optical fiber. Nat. Neurosci. *20*, 1180–1188.

Pisano, F., Pisanello, M., Lee, S.J., Lee, J., Maglie, E., Balena, A., Sileo, L., Spagnolo, B., Bianco, M., Hyun, M., et al. (2019). Depth-resolved fiber photometry with a single tapered optical fiber implant. Nat. Methods *16*, 1185–1192.

Pnevmatikakis, E.A., Soudry, D., Gao, Y., Machado, T.A., Merel, J., Pfau, D., Reardon, T., Mu, Y., Lacefield, C., Yang, W., et al. (2016). Simultaneous Denoising, Deconvolution, and Demixing of Calcium Imaging Data. Neuron *89*, 285–299.

Power, R.M., and Huisken, J. (2017). A guide to light-sheet fluorescence microscopy for multiscale imaging. Nat. Methods *14*, 360–373.

Puszka, A., Di Sieno, L., Mora, A.D., Pifferi, A., Contini, D., Boso, G., Tosi, A., Hervé, L., Planat-Chrétien, A., Koenig, A., and Dinten, J.M. (2013). Time-resolved diffuse optical tomography using fast-gated single-photon avalanche diodes. Biomed. Opt. Express *4*, 1351–1365.

Ravotto, L., Duffet, L., Zhou, X., Weber, B., and Patriarchi, T. (2020). A Bright and Colorful Future for G-Protein Coupled Receptor Sensors. Front. Cell. Neurosci. *14*, 67.

Reece, M., and O'Keefe, J. (1989). The tetrode: A new technique for multiunit extracellular recording. Soc. Neurosci. Abstr. *15*, 1270.

Resink, S.G., Boccara, A.C., and Steenbergen, W. (2012). State-of-the art of acousto-optic sensing and imaging of turbid media. J. Biomed. Opt. *17*, 040901.

Rios, G., Lubenov, E.V., Chi, D., Roukes, M.L., and Siapas, A.G. (2016). Nanofabricated Neural Probes for Dense 3-D Recordings of Brain Activity. Nano Lett. *16*, 6857–6862.

Roukes, M.L. (2011). Brain-machine interface based on photonic neural probe arrays. US patent 10638933, filed May 22, 2017, and granted May 5, 2020.

Roukes, M.L., Cotton, R.J., Moreaux, L.C., Shepard, K.L., Siapas, A., and Tolias, A. (2016). One-photon integrated neurophotonic systems. US patent application publication 20160150963, filed November 5, 2014, and published June 2, 2016.

Rousche, P.J., Pellinen, D.S., Pivin, D.P., Jr., Williams, J.C., Vetter, R.J., and Kipke, D.R. (2001). Flexible polyimide-based intracortical electrode arrays with bioactive capability. IEEE Trans. Biomed. Eng. *48*, 361–371.

Rungta, R.L., Osmanski, B.F., Boido, D., Tanter, M., and Charpak, S. (2017). Light controls cerebral blood flow in naive animals. Nat. Commun. *8*, 14191.

Rustami, E., Sasagawa, K., Sugie, K., Ohta, Y., Haruta, M., Noda, T., Tokuda, T., and Ohta, J. (2020). Needle-Type Imager Sensor with Band-Pass Composite Emission Filter and Parallel Fiber-Coupled Laser Excitation. IEEE Transactions on Circuits and Systems I: Regular Papers *67*, 1082–1091.

Sacher, W.D., Mikkelsen, J.C., Dumais, P., Jiang, J., Goodwill, D., Luo, X., Huang, Y., Yang, Y., Bois, A., Lo, P.G., et al. (2017). Tri-layer silicon nitride-on-silicon photonic platform for ultra-low-loss crossings and interlayer transitions. Opt. Express *25*, 30862–30875.

Sacher, W.D., Chen, F.D., Moradi-Chameh, H., Luo, X., Fomenko, A., Shah, P., Lordello, T., Liu, X., Felts Almog, I., Straguzzi, J.N., et al. (2020). Implantable photonic neural probes for light-sheet fluorescence brain imaging. bioRxiv. https://doi.org/10.1101/2020.09.27.315556.

Sacher, W.D., Liu, X.Y., Almog, I.F., Fomenko, A., Lordello, T., Chen, F.D., Moradi-Chameh, H., Naderian, A., Chang, M., Fowler, T.M., et al. (2019a). Nanophotonic neural probes for in vivo light sheet imaging. In Conference on Lasers and Electro-Optics (Optical Society of America), paper SM4H.6.

Sacher, W.D., Liu, X.Y., Chen, F.D., Moradi-Chameh, H., Almog, I.F., Lordello, T., Chang, M., Naderian, A., Fowler, T.M., Segev, E., et al. (2019b). Beam-steering nanophonic phased-array neural probes. In Conference on Lasers and Electo-Optics (Optical Society of America), paper ATh4I.4.

Sacher, W.D., Luo, X., Yang, Y., Chen, F.D., Lordello, T., Mak, J.C.C., Liu, X., Hu, T., Xue, T., Guo-Qiang Lo, P., et al. (2019c). Visible-light silicon nitride waveguide devices and implantable neurophotonic probes on thinned 200 mm silicon wafers. Opt. Express *27*, 37400–37418.

Sasagawa, K., Kimura, A., Haruta, M., Noda, T., Tokuda, T., and Ohta, J. (2018). Highly sensitive lens-free fluorescence imaging device enabled by a complementary combination of interference and absorption filters. Biomed. Opt. Express *9*, 4329–4344.

Segev, E., Moreaux, L.M., Fowler, T.M., Faraon, A., and Roukes, M.L. (2015). Implantable, highly collimated light-emitters for biological applications, US patent 10471273, filed October 17, 2016, and granted November 12, 2019.

Segev, E., Reimer, J., Moreaux, L.C., Fowler, T.M., Chi, D., Sacher, W.D., Lo, M., Deisseroth, K., Tolias, A.S., Faraon, A., and Roukes, M.L. (2017). Patterned photostimulation via visible-wavelength photonic probes for deep brain optogenetics. Neurophotonics *4*, 011002.

Senova, S., Scisniak, I., Chiang, C.-C., Doignon, I., Palfi, S., Chaillet, A., Martin, C., and Pain, F. (2017). Experimental assessment of the safety and potential efficacy of high irradiance photostimulation of brain tissues. Sci. Rep. *7*, 43997.

Shahrjerdi, D., and Bedell, S.W. (2013). Extremely flexible nanoscale ultrathin body silicon integrated circuits on plastic. Nano Lett. *13*, 315–320.

Shao, Z., Chen, Y., Chen, H., Zhang, Y., Zhang, F., Jian, J., Fan, Z., Liu, L., Yang, C., Zhou, L., and Yu, S. (2016). Ultra-low temperature silicon nitride photonic integration platform. Opt. Express *24*, 1865–1872.

Shemesh, O.A., Linghu, C., Piatkevich, K.D., Goodwin, D., Celiker, O.T., Gritton, H.J., Romano, M.F., Gao, R., Yu, C.J., Tseng, H.A., et al. (2020). Precision Calcium Imaging of Dense Neural Populations via a Cell-Body-Targeted Calcium Indicator. Neuron *107*, 470–486.e11.

Shichida, Y., and Matsuyama, T. (2009). Evolution of opsins and phototransduction. Philos. Trans. R. Soc. Lond. B Biol. Sci. *364*, 2881–2895.

Shobe, J.L., Claar, L.D., Parhami, S., Bakhurin, K.I., and Masmanidis, S.C. (2015). Brain activity mapping at multiple scales with silicon microprobes containing 1,024 electrodes. J. Neurophysiol. *114*, 2043–2052.

Shuman, T., Aharoni, D., Cai, D.J., Lee, C.R., Chavlis, S., Page-Harley, L., Vetere, L.M., Feng, Y., Yang, C.Y., Mollinedo-Gajate, I., et al. (2020). Breakdown

of spatial coding and interneuron synchronization in epileptic mice. Nat. Neurosci. *23*, 229–238.

Sileo, L., Bitzenhofer, S.H., Spagnolo, B., Pöpplau, J.A., Holzhammer, T., Pisanello, M., Pisano, F., Bellistri, E., Maglie, E., De Vittorio, M., et al. (2018). Tapered Fibers Combined With a Multi-Electrode Array for Optogenetics in Mouse Medial Prefrontal Cortex. Front. Neurosci. *12*, 771.

Skocek, O., Nöbauer, T., Weilguny, L., Martínez Traub, F., Xia, C.N., Molodtsov, M.I., Grama, A., Yamagata, M., Aharoni, D., Cox, D.D., et al. (2018). High-speed volumetric imaging of neuronal activity in freely moving rodents. Nat. Methods *15*, 429–432.

Sofroniew, N.J., Flickinger, D., King, J., and Svoboda, K. (2016). A large field of view two-photon mesoscope with subcellular resolution for in vivo imaging. eLife *5*, 5.

Sriram, S., Partlow, W.D., and Liu, C.S. (1983). Low-loss optical waveguides using plasma-deposited silicon nitride. Appl. Opt. *22*, 3664–3665.

Steinmetz, N.A., Koch, C., Harris, K.D., and Carandini, M. (2018). Challenges and opportunities for large-scale electrophysiology with Neuropixels probes. Curr. Opin. Neurobiol. *50*, 92–100.

Steinmetz, N.A., Zatka-Haas, P., Carandini, M., and Harris, K.D. (2019). Distributed coding of choice, action and engagement across the mouse brain. Nature *576*, 266–273.

Stevenson, I.H., and Kording, K.P. (2011). How advances in neural recording affect data analysis. Nat. Neurosci. *14*, 139–142.

Sun, F., Zeng, J., Jing, M., Zhou, J., Feng, J., Owen, S.F., Luo, Y., Li, F., Wang, H., Yamaguchi, T., et al. (2018). A Genetically Encoded Fluorescent Sensor Enables Rapid and Specific Detection of Dopamine in Flies, Fish, and Mice. Cell *174*, 481–496.e19.

Thompson, S.M., Masukawa, L.M., and Prince, D.A. (1985). Temperature dependence of intrinsic membrane properties and synaptic potentials in hippocampal CA1 neurons in vitro. J. Neurosci. *5*, 817–824.

Tian, L., Hires, S.A., Mao, T., Huber, D., Chiappe, M.E., Chalasani, S.H., Petreanu, L., Akerboom, J., McKinney, S.A., Schreiter, E.R., et al. (2009). Imaging neural activity in worms, flies and mice with improved GCaMP calcium indicators. Nat. Methods *6*, 875–881.

Ulku, A.C., Bruschini, C., Antolovic, I.M., Charbon, E., Kuo, Y., Ankri, R., Weiss, S., and Michalet, X. (2019). A 512×512 SPAD Image Sensor with Integrated Gating for Widefield FLIM. IEEE J. Sel. Top. Quantum Electron. *25*, 25.

Villette, V., Chavarha, M., Dimov, I.K., Bradley, J., Pradhan, L., Mathieu, B., Evans, S.W., Chamberland, S., Shi, D., Yang, R., et al. (2019). Ultrafast Two-Photon Imaging of a High-Gain Voltage Indicator in Awake Behaving Mice. Cell *179*, 1590–1608.e23.

Voleti, V., Patel, K.B., Li, W., Perez Campos, C., Bharadwaj, S., Yu, H., Ford, C., Casper, M.J., Yan, R.W., Liang, W., et al. (2019). Real-time volumetric microscopy of in vivo dynamics and large-scale samples with SCAPE 2.0. Nat. Methods *16*, 1054–1062.

Walker, E.Y., Sinz, F.H., Cobos, E., Muhammad, T., Froudarakis, E., Fahey, P.G., Ecker, A.S., Reimer, J., Pitkow, X., and Tolias, A.S. (2019). Inception loops discover what excites neurons most using deep predictive models. Nat. Neurosci. *22*, 2060–2065.

Wang, L.V. (2001). Mechanisms of ultrasonic modulation of multiply scattered coherent light: an analytic model. Phys. Rev. Lett. *87*, 043903.

Wang, L., and Zhao, X. (1997). Ultrasound-modulated optical tomography of absorbing objects buried in dense tissue-simulating turbid media. Appl. Opt. *36*, 7277–7282.

Wang, X.F., Uchida, T., Coleman, D.M., and Minami, S. (1991). A two-dimensional fluorescence lifetime imaging system using a gated image intensifier. Appl. Spectrosc. *45*, 360–366.

Wang, L., Jacques, S.L., and Zhao, X. (1995). Continuous-wave ultrasonic modulation of scattered laser light to image objects in turbid media. Opt. Lett. *20*, 629–631.

Wang, H., Dewell, R.B., Ehrengruber, M.U., Segev, E., Reimer, J., Roukes, M.L., and Gabbiani, F. (2018). Optogenetic manipulation of medullary neurons in the locust optic lobe. J. Neurophysiol. *120*, 2049–2058.

Wang, A., Gill, P., and Molnar, A. (2009). Light field image sensors based on the Talbot effect. Appl. Opt. *48*, 5897–5905.

Wang, M., Wu, C., Sinefeld, D., Li, B., Xia, F., and Xu, C. (2018). Comparing the effective attenuation lengths for long wavelength in vivo imaging of the mouse brain. Biomed. Opt. Express *9*, 3534–3543.

Wheelock, M.D., Culver, J.P., and Eggebrecht, A.T. (2019). High-density diffuse optical tomography for imaging human brain function. Rev. Sci. Instrum. *90*, 051101.

Wilson, M.A., and McNaughton, B.L. (1993). Dynamics of the hippocampal ensemble code for space. Science *261*, 1055–1058.

Wise, K.D., Angell, J.B., and Starr, A. (1970). An integrated-circuit approach to extracellular microelectrodes. IEEE Trans. Biomed. Eng. *17*, 238–247.

Wise, K.D., Sodagar, A.M., Yao, Y., Gulari, M.N., Gayatri, E.P., and Najafi, K. (2008). Microelectrodes, microelectronics, and implantable neural microsystems. Proceedings of the IEEE *96*, 1184–1202.

Wu, F., Stark, E., Ku, P.C., Wise, K.D., Buzsáki, G., and Yoon, E. (2015). Monolithically Integrated μLEDs on Silicon Neural Probes for High-Resolution Optogenetic Studies in Behaving Animals. Neuron *88*, 1136–1148.

Wu, J., Liang, Y., Chen, S., Hsu, C.L., Chavarha, M., Evans, S.W., Shi, D., Lin, M.Z., Tsia, K.K., and Ji, N. (2020). Kilohertz two-photon fluorescence microscopy imaging of neural activity in vivo. Nat. Methods *17*, 287–290.

Xu, M., and Wang, L.V. (2006). Photoacoustic imaging in biomedicine. Rev. Sci. Instrum. *77*, 041101.

Yaqoob, Z., Psaltis, D., Feld, M.S., and Yang, C. (2008). Optical Phase Conjugation for Turbidity Suppression in Biological Samples. Nat. Photonics *2*, 110–115.

Yatsenko, D., Moreaux, L.C., Choi, J., Tolias, A.S., Shepard, K.L., and Roukes, M.L. (2020). Signal separability in integrated neurophotonics. bioRxiv. https://doi.org/10.1101/2020.09.27.315556.

Ye, F., Avants, B.W., and Robinson, J.T. (2016). Light sheet illumination with an integrated photonic probe. In Conference on Lasers and Electro-Optics (Optical Society of America), paper JW2A142.

Yuste, R. (2010). Imaging: A Laboratory Manual (Cold Spring Harbor Laboratory Press).

Yuste, R., and Katz, L.C. (1991). Control of postsynaptic Ca2+ influx in developing neocortex by excitatory and inhibitory neurotransmitters. Neuron *6*, 333–344.

Zhang, F., Aravanis, A.M., Adamantidis, A., de Lecea, L., and Deisseroth, K. (2007). Circuit-breakers: optical technologies for probing neural signals and systems. Nat. Rev. Neurosci. *8*, 577–581.

Zhou, P., Resendez, S.L., Rodriguez-Romaguera, J., Jimenez, J.C., Neufeld, S.Q., Giovannucci, A., Friedrich, J., Pnevmatikakis, E.A., Stuber, G.D., Hen, R., et al. (2018). Efficient and accurate extraction of in vivo calcium signals from microendoscopic video data. eLife *7*, e28728.

Zong, W., Wu, R., Li, M., Hu, Y., Li, Y., Li, J., Rong, H., Wu, H., Xu, Y., Lu, Y., et al. (2017). Fast high-resolution miniature two-photon microscopy for brain imaging in freely behaving mice. Nat. Methods *14*, 713–719.

Zorzos, A.N., Scholvin, J., Boyden, E.S., and Fonstad, C.G. (2012). Three-dimensional multiwaveguide probe array for light delivery to distributed brain circuits. Opt. Lett. *37*, 4841–4843.